

# 1 Highlights

## 2 **A distributed activation energy model for clumped isotope bond reordering in carbonates**

3 Jordon D. Hemingway, Gregory A. Henkes

- 4 • Carbonate clumped isotope ratios can be overprinted during diagenesis & metamorphism
- 5 • We model carbonate clumped isotope bond reordering using a disordered kinetic approach
- 6 • All previous models are shown to be specific cases of disordered kinetics
- 7 • Calcite & dolomite rate coefficient distributions are well-approximated as lognormal
- 8 • Geologically relevant heating/cooling examples can contextualize natural measurements

# A distributed activation energy model for clumped isotope bond reordering in carbonates

Jordon D. Hemingway<sup>a,1,\*</sup>, Gregory A. Henkes<sup>b,1,\*</sup>

<sup>a</sup>Department of Earth and Planetary Sciences, Harvard University, Cambridge, Massachusetts, USA

<sup>b</sup>Department of Geosciences, Stony Brook University, Stony Brook, New York, USA

---

## Abstract

Carbonate clumped isotopes ( $\Delta_{47}$ ) have become a widely applied method for paleothermometry, with applications spanning many environmental settings over hundreds of millions of years. However,  $\Delta_{47}$ -based paleothermometry can be complicated by closure temperature-like behavior whereby C–O bonds are reset at elevated diagenetic or metamorphic temperatures, sometimes without obvious mineral alteration. Laboratory studies have constrained this phenomenon by heating well-characterized materials at various temperatures, observing temporal  $\Delta_{47}$  evolution, and fitting results to kinetic models with prescribed C–O bond reordering mechanisms. While informative, these models are inflexible regarding the nature of isotope exchange, leading to potential uncertainties when extrapolated to geologic timescales. Here, we propose a “disordered” kinetic framework to circumvent this issue by modeling C–O bond reordering as a continuum of first-order processes occurring in parallel at different rates. We show theoretically that all previous models are specific cases of disordered kinetics; thus, our approach reconciles the transient defect/equilibrium defect and paired reaction-diffusion models. We estimate the rate coefficient distributions from published heating experiment data by finding a regularized inverse solution that best fits each  $\Delta_{47}$  timeseries. Importantly, this approach does not assume a particular mechanism or energy distribution *a priori*. Resulting distributions are well-approximated as lognormal for all experiments on calcite or dolomite; aragonite experiments require more complex distributions. Presuming lognormal rate coefficient distributions and Arrhenius-like temperature dependence yields an underlying activation energy,  $E$ , distribution that is Gaussian with a mean value of  $\mu_E = 224.3 \pm 27.6$  kJ mol<sup>-1</sup> and a standard deviation of  $\sigma_E = 17.4 \pm 0.7$  kJ mol<sup>-1</sup> ( $\pm 1\sigma$  uncertainty;  $n = 24$ ) for calcite and  $\mu_E = 230.3 \pm 47.7$  kJ mol<sup>-1</sup> and  $\sigma_E = 14.8 \pm 2.2$  kJ mol<sup>-1</sup> ( $n = 4$ ) for dolomite. These model results are adaptable to other minerals and may provide a basis for future experiments whereby the nature of carbonate C–O bonds is altered (e.g., by inducing mechanical strain or cation substitution). Finally, we apply our results to geologically relevant heating/cooling histories and suggest that previous models underestimate low-temperature alteration but overestimate  $\Delta_{47}$  blocking temperatures.

**Keywords:** activation energy model, carbonate, apparent equilibrium temperature, clumped isotopes, solid-state diffusion, thermometry

## 39 1. Introduction

40 Carbonate clumped isotope ratios (reported as  $\Delta_{47}$ ) are a valuable paleothermometer because they have been  
41 shown—empirically and experimentally—to solve the underdetermination problem with carbonate-water oxygen iso-  
42 tope exchange thermometry (Eiler, 2011). This apparent panacea, however, comes with caveats. Specifically, clumped  
43 isotopes are subject to alteration during diagenetic dissolution-reprecipitation of the original carbonate, both in water-  
44 buffered and rock-buffered settings (e.g., Huntington et al., 2011; Ryb and Eiler, 2018; Shenton et al., 2015), and  
45 by internal, diffusion-driven isotope exchange reactions within the solid mineral lattice at elevated temperatures—so-  
46 called “solid-state clumped isotope bond reordering” (Dennis and Schrag, 2010; Passey and Henkes, 2012; Stolper  
47 and Eiler, 2015; Brenner et al., 2018; Lloyd et al., 2018; Chen et al., 2019).

48 Bond reordering has been observed or hypothesized to affect carbonates from virtually every geologic context  
49 in which they are found on Earth. Empirical evidence comes from two main sources: (i) carbonatites, where  $\Delta_{47}$ -  
50 derived temperatures,  $T(\Delta_{47})$ , are consistently much lower than inferred igneous crystallization temperatures (Dennis  
51 and Schrag, 2010; Stolper and Eiler, 2015; Fosu et al., 2020), and (ii) marbles and sedimentary rock alteration along  
52 dikes, where  $T(\Delta_{47})$  systematically increases closer to the heat source (Finnegan et al., 2011; Ferry et al., 2011;  
53 Lloyd et al., 2017; Ryb et al., 2017). Furthermore, bond reordering has been invoked to explain elevated  $T(\Delta_{47})$  in  
54 deeply buried paleoclimate archives (e.g., shells and carbonate nodules) that were petrographically and geochemically  
55 well-preserved (e.g., Quade et al., 2013; Shenton et al., 2015; Henkes et al., 2014, 2018). Predicting the impact  
56 of bond reordering on measured  $\Delta_{47}$  values is thus critically important for properly interpreting clumped isotope  
57 paleotemperature records, particularly in older archives that may have been exposed to higher diagenetic temperatures  
58 (Henkes et al., 2018).

59 Quantifying bond reordering necessitates kinetic models that both satisfy experimental tests and are amenable to  
60 a wide range of geologic applications. This has been achieved in the laboratory by heating the same mineralogically  
61 pure carbonate material at multiple temperatures for discrete time intervals. From these studies, it is possible to  
62 observe  $\Delta_{47}$  evolution without obvious physical or bulk isotopic changes to the reactant (i.e., decarbonation or mineral-  
63 gas/mineral-liquid isotope exchange). By assuming first-order kinetics and Arrhenius-like temperature dependence,  
64 one can utilize heating experiment results to estimate  $E$ , the underlying activation energy of clumped isotope bond  
65 reordering (Passey and Henkes, 2012; Stolper and Eiler, 2015). Though the large effort required for these experiments  
66 has limited the extent of comparisons, previous models concluded that  $E$  values for all studied types of calcite (i.e.,  
67 optical calcite, brachiopod shells) are statistically indistinguishable (Henkes et al., 2014; Stolper and Eiler, 2015).  
68 Similarly, while the presence of water at high pressure does increase the Arrhenius pre-exponential factor  $k_0$  and thus  
69 the overall reaction rate, it does not appear to influence calcite  $E$  values, consistent with the inferred dependence on

---

\*Corresponding authors

*Email addresses:* jordon\_hemingway@fas.harvard.edu (Jordon D. Hemingway), gregory.henkes@stonybrook.edu (Gregory A. Henkes)

<sup>1</sup>These authors contributed equally to this work

70 bulk diffusivity (Brenner et al., 2018). Thus, given experimentally determined  $E$  and  $k_0$  values, one can estimate  $\Delta_{47}$   
71 evolution due to bond reordering for any carbonate sample that has experienced any specified time-temperature ( $t$ - $T$ )  
72 history (Passey and Henkes, 2012; Stolper and Eiler, 2015).

73 However, nearly all heating experiments to date are complicated by the presence of an early, rapid change in  $\Delta_{47}$   
74 that appears to deviate from first-order behavior (Passey and Henkes, 2012; Henkes et al., 2014; Stolper and Eiler,  
75 2015; Lloyd et al., 2018). While initially ignored, these early data points have since prompted the development of  
76 two alternative bond reordering models. First, the so-called "transient defect/equilibrium defect" model of Henkes  
77 et al. (2014) posits that non-first order behavior results from the simultaneous reaction of two defect populations:  
78 one that follows first-order kinetics and a second whose concentration decreases with prolonged heating. Despite  
79 its presence, Passey and Henkes (2012) and Henkes et al. (2014) argue that the nature of this transient defect pool is  
80 ambiguous and likely unimportant in many geologic contexts. Second, the so-called "paired reaction-diffusion" model  
81 of Stolper and Eiler (2015) treats the early, rapid change in experimental  $\Delta_{47}$  as the result of interactions between pairs  
82 of neighboring, singly substituted carbonate groups; these groups can then diffuse through the crystal lattice according  
83 to first-order kinetics. This model is intuitive and capable of capturing  $\Delta_{47}$  changes in most experimental datasets but  
84 is inflexible and disregards the contribution of lattice defects or other extrinsic factors that may promote (or quench)  
85 isotope exchange. Importantly, both models prescribe C–O bond reordering mechanisms *a priori*, potentially leading  
86 to large uncertainties when extrapolated to geologic  $t$ - $T$  histories.

87 To obviate the need for *a priori* mechanistic assumptions, here we recast clumped isotope bond reordering as a  
88 so-called "disordered" kinetic process whereby solid state C–O isotope exchange occurs as a parallel superposition of  
89 first-order reactions. We show theoretically that all previously published models represent specific cases of disordered  
90 kinetics subject to certain constraints. We then relax these constraints and estimate the distributions of rate coefficients  
91 that best fit experimental data using a regularized inverse approach. Resulting rate coefficient distributions are gener-  
92 ally well-approximated as lognormal, indicating that underlying  $E$  distributions are Gaussian, consistent with the  
93 central limit theorem. Finally, we compare our bond reordering predictions to those of previous models and estimate  
94  $\Delta_{47}$  evolution for examples of geologically relevant heating/cooling histories.

## 95 **2. Methods**

### 96 *2.1. Data compilation*

97 To develop our model, we compiled results from all published experiments designed to derive the kinetics of  
98 solid-state C–O bond reordering. This includes  $\Delta_{47}$  data from 42 experiments using four carbonate minerals: optical  
99 and fossil brachiopod calcite (Passey and Henkes, 2012; Henkes et al., 2014; Stolper and Eiler, 2015; Brenner et al.,  
100 2018), aragonite (Chen et al., 2019), stoichiometric dolomite (Lloyd et al., 2018), and the carbonate group within ap-  
101 atite (Stolper and Eiler, 2015). All data were generated using near-identical analytical methods either at the California  
102 Institute of Technology (see Passey et al., 2010) or at Johns Hopkins University (see Henkes et al., 2013). To summa-

103 rize, this included carbonate digestion using a 90 °C common phosphoric acid bath, CO<sub>2</sub> purification by cryogenic and  
 104 He-carrier gas chromatography using a Pora-pak Q column, and measurement of *m/z* 44–49 on a Thermo Scientific  
 105 MAT 253 isotope ratio mass spectrometer. Reported clumped isotope compositions are then calculated as

$$\Delta_{47} = \left[ \left( \frac{R^{47}}{R^{*47}} - 1 \right) - \left( \frac{R^{46}}{R^{*46}} - 1 \right) - \left( \frac{R^{45}}{R^{*45}} - 1 \right) \right] \times 1000\text{‰}, \quad (1)$$

106 where  $R^i$  is the measured ratio of isotopologue  $i$  relative to <sup>12</sup>C<sup>16</sup>O<sub>2</sub> and  $R^{*i}$  is the predicted ratio of isotopologue  $i$   
 107 relative to <sup>12</sup>C<sup>16</sup>O<sub>2</sub> if all isotopes were randomly distributed (Affek and Eiler, 2006).

108 To perform all calculations in a standardized reference frame, we refer to only published data on the “carbon  
 109 dioxide equilibrium scale” (Dennis et al., 2011) uncorrected for the fractionation factor between 25 °C and 90 °C  
 110 phosphoric acid reaction (i.e., CDES<sub>90</sub>; Bonifacie et al., 2017). Study-specific fractionation factors were used to  
 111 uncorrect all data except those presented in Stolper and Eiler (2015); since no fractionation factor was reported for  
 112 these experiments, a value of 0.092 ‰ was used to match that reported for other data generated in the same laboratory  
 113 during the same time period (e.g., Bonifacie et al., 2017). Isotopologue reordering reaction progress should be  
 114 insensitive to the reported  $\Delta_{47}$  values (i.e., acid or any other standardized correction) so long as equilibrium  $\Delta_{47}$  is  
 115 reported in the same reference frame. We thus made no attempt to correct for differences in isotope parameters used  
 116 between studies (but see Daëron et al., 2016, for isotope parameter discussion).

117 Assessing model fits requires knowledge of measurement uncertainty. Here, we use  $\Delta_{47}$  uncertainty reported in  
 118 each original study without further correction. For samples with replicate measurements, reported uncertainty is the  
 119  $\pm 1$  standard error (s.e.) of all replicates. For samples analyzed only once, reported uncertainty is typically equal to  
 120 the long-term instrument precision of a suite of standards (Passey et al., 2010; Henkes et al., 2013). In the compiled  
 121 dataset, uncertainty averages  $\pm 0.013$  ‰ and never exceeds 0.041 ‰ ( $n = 355$ ).

122 All stable isotope data are presented in Table S.1, including: published  $\delta^{13}\text{C}$ ,  $\delta^{18}\text{O}$ , and  $\Delta_{47}$  values;  $\Delta_{47}$  values  
 123 after conversion to the CDES<sub>90</sub> reference frame; and  $\Delta_{47}$  uncertainty.

## 124 2.2. Data analysis

125 Determining C–O bond reordering progress requires knowledge of  $\Delta_{47}^{\text{eq}}(T)$ , the equilibrium  $\Delta_{47}$  value at each  
 126 experimental temperature. Here, we calculate  $\Delta_{47}^{\text{eq}}(T)$  using the multiple mineralogy high-temperature  $T$  vs.  $\Delta_{47}^{\text{eq}}(T)$   
 127 calibration equation of Bonifacie et al. (2017) (their Eq. 2). This equation is remarkably similar both to previous  
 128 equations calibrated to calcite only (Passey and Henkes, 2012, corrected to CDES<sub>90</sub>) and to theoretical predictions  
 129 after accounting for acid fractionation (Schauble et al., 2006); it is therefore recommended for all high-temperature  
 130 calibrations independent of mineralogy (Bonifacie et al., 2017). However, Lloyd et al. (2018) advocate for the theo-  
 131 retical calibration equation of Schauble et al. (2006) (corrected to CDES<sub>90</sub>) for dolomite reordering experiments since  
 132 the Bonifacie et al. (2017) calibration over-estimates measured high-temperature dolomite  $\Delta_{47}^{\text{eq}}(T)$  values by up to  
 133 0.015 ‰. For consistency, we retain the Bonifacie et al. (2017) calibration for all calculations performed herein, and  
 134 we discuss in Section 4.3 the degree to which this choice influences resulting activation energy estimates.

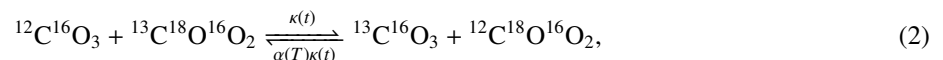
135 All calculations were performed using the 'isotopylog' package in Python 3.7 (Hemingway, 2020). Regularized  
136 inversion solutions (Section 3.2.1) were determined using the non-negative least squares algorithm in Lawson and  
137 Hanson (1995), whereas lognormal rate distribution solutions (Section 3.2.2) and Arrhenius parameters (Section 3.3),  
138 including error estimation, were determined using the Levenberg-Marquardt algorithm for non-linear curve fitting  
139 with each data point weighted by the inverse of its analytical variance (Marquardt, 1963). Python scripts to generate  
140 all figures and tables are included in the supplementary information.

### 141 3. Theory

142 In this section, we first derive the disordered kinetic model and show that this naturally leads to the  $\Delta_{47}$  evolu-  
143 tion slowdown observed during carbonate heating experiments (Section 3.1). In doing so, we demonstrate that the  
144 "pseudo-first-order" (Passey and Henkes, 2012), "transient/equilibrium-defect" (Henkes et al., 2014), and "paired  
145 reaction-diffusion" (Stolper and Eiler, 2015) models all represent specific cases of disordered kinetics. We further  
146 describe how this framework can explain non-monotonic  $\Delta_{47}$  evolution, as has been observed in aragonite heating  
147 experiments (Chen et al., 2019). Second, we outline an inversion approach to determine the rate distributions that  
148 best fit experimental data, and we show that these distributions are approximately lognormal (Section 3.2). Finally,  
149 we estimate the underlying activation energy distributions using an Arrhenius approach (Section 3.3) and show how  
150 to calculate  $\Delta_{47}$  evolution—including uncertainty propagation—over geologically relevant time-temperature histories  
151 (Section 3.4). For reference, all mathematical symbols are described in Table S.2.

#### 152 3.1. Theoretical derivation

153 The carbonate isotopologue reordering reaction can be written as



154 where  $\kappa(t)$  is the apparent rate coefficient of the "order-to-disorder" reaction at time  $t$  and  $\alpha(T)$  is the temperature-  
155 dependent equilibrium constant (Passey and Henkes, 2012). A general feature of all carbonate isotopologue reordering  
156 experiments is that  $\kappa(t)$  decreases with time, either monotonically (e.g., apatite, calcite, dolomite; Passey and Henkes,  
157 2012; Henkes et al., 2014; Stolper and Eiler, 2015; Brenner et al., 2018; Lloyd et al., 2018) or after early transient  
158 features have dissipated (e.g., aragonite; Chen et al., 2019).

159 A decreasing apparent rate coefficient can be shown to result from a superposition of multiple reactions, each  
160 following a unique rate coefficient  $k$  (Huber, 1985; Ross and Vlad, 1999). This approach is commonly applied to  
161 disordered systems such as organic carbon remineralization (Boudreau and Ruddick, 1991; Forney and Rothman,  
162 2012a; Hemingway et al., 2017), fossil fuel pyrolysis (Burnham and Braun, 1999), and nonlinear chemical kinetics  
163 (Huber, 1985; Ross and Vlad, 1999). Here, we suppose that carbonate  $\Delta_{47}$  evolution during isotopologue reordering  
164 similarly follows disordered kinetics. We define the normalized deviation from equilibrium for a subset of material

165 that is associated with a given rate coefficient  $k$  at time  $t$  as

$$g(k, t) = \frac{\Delta_{47}(k, t) - \Delta_{47}^{\text{eq}}(T)}{\Delta_{47}^0 - \Delta_{47}^{\text{eq}}(T)}, \quad (3)$$

166 where  $\Delta_{47}(k, t)$  is the  $\Delta_{47}$  value of material associated with rate  $k$  at time  $t$ ,  $\Delta_{47}^0$  is the measured  $\Delta_{47}$  value at  $t = 0$ , and  
 167  $\Delta_{47}^{\text{eq}}(T)$  is the temperature-dependent equilibrium  $\Delta_{47}$  value;  $\Delta_{47}^{\text{eq}}(T)$  can be measured empirically (Ghosh et al., 2006;  
 168 Passey and Henkes, 2012; Bonifacie et al., 2017) or determined theoretically using first-principles estimates of  $\alpha(T)$   
 169 (Schauble et al., 2006).

170 Following Passey and Henkes (2012), we show in Appendix A that  $g(k, t)$  evolves with time as

$$g(k, t) = e^{-kt}. \quad (4)$$

171 That is,  $g(k, t)$  follows first-order kinetics. We similarly define the normalized deviation from equilibrium for the bulk  
 172 sample at time  $t$  as

$$G(t) = \frac{\Delta_{47}(t) - \Delta_{47}^{\text{eq}}(T)}{\Delta_{47}^0 - \Delta_{47}^{\text{eq}}(T)}, \quad (5)$$

173 where  $\Delta_{47}(t)$  is the measured  $\Delta_{47}$  value at time  $t$ . By assuming disordered kinetics, it follows that  $G(t)$  evolves as a  
 174 superposition of first-order reactions:

$$G(t) = \int_0^{\infty} p(k)g(k, t)dk, \quad (6)$$

175 where  $p(k)$  is the fraction of total material initially associated with rate coefficient  $k$  such that  $p(k) \geq 0$  for all  $k$  and

$$\int_0^{\infty} p(k) \equiv 1. \quad (7)$$

176 That is,  $p(k)$  forms a probability density function (pdf). Substituting Eq. 4 into Eq. 6 yields

$$G(t) = \int_0^{\infty} p(k)e^{-kt} dk, \quad (8)$$

177 which defines the Laplace transform of  $p(k)$  (Hansen, 1994; Forney and Rothman, 2012a). Because the superposition  
 178 of parallel first-order reactions is itself first order, it follows that

$$\frac{dG(t)}{dt} = -\kappa(t)G(t), \quad (9)$$

179 where  $\kappa(t)$  is the apparent rate coefficient at time  $t$  (Eq. 1). Combining Eqs. 8 and 9 yields

$$\kappa(t) = \frac{\int_0^{\infty} kp(k)e^{-kt} dk}{\int_0^{\infty} p(k)e^{-kt} dk}, \quad (10)$$

180 which defines the arithmetic mean of  $k$  weighted by  $p(k)e^{-kt}$ . Equation 10 states that small  $k$  values become more  
 181 heavily weighted with increasing  $t$  since  $e^{-kt}$  approaches zero most rapidly for large  $k$ . Put differently,  $\kappa(t)$  must  
 182 decrease with time for any distribution of  $p(k)$  other than a single delta function [in which case  $\kappa(t)$  is constant; see  
 183 Section 3.1.1]. The observed decrease in  $\kappa(t)$ , which prompted the development of the transient/equilibrium-defect  
 184 (Henkes et al., 2014) and paired reaction-diffusion (Stolper and Eiler, 2015) models, is thus a natural consequence of  
 185 disordered kinetics. We now demonstrate that Eq. 8 can describe all previous isotopologue reordering models given  
 186 the right choice of  $p(k)$ .

187 *3.1.1. Relationship to previous models: Passey and Henkes (2012)*

188 We first consider the "pseudo-first-order" model, which supposes that reordering after some critical time point  $t_{cr}$   
 189 follows a single first-order reaction with rate constant  $k_c$ . This is written mathematically as a delta function, which  
 190 has the properties

$$\delta(k - k_c) = \begin{cases} \infty, & \text{if } k = k_c \\ 0, & \text{otherwise} \end{cases} \quad (11)$$

191 and

$$\int_{-\infty}^{\infty} \delta(k - k_c) dk = 1. \quad (12)$$

192 Reaction progress for  $t < t_{cr}$  is ignored since it is hypothesized to include "transient defects" that are an artifact of  
 193 experimental heating. We thus define  $\tau = t - t_{cr}$  and  $p(k) = \delta(k - k_c)$ . Equation 8 becomes

$$\begin{aligned} G(\tau) &= \int_0^{\infty} \delta(k - k_c) e^{-k\tau} dk, \\ &= e^{-k_c\tau}, \end{aligned} \quad (13)$$

194 which is identical to governing equation of Passey and Henkes (2012) (their Eq. 3). It can be similarly shown from  
 195 Eq. 10 that  $\kappa(\tau) = k_c$  for all  $\tau$ , as expected.

196 *3.1.2. Relationship to previous models: Henkes et al. (2014)*

197 Next, we consider the "transient defect/equilibrium defect" model. This is an extension of the pseudo-first-order  
 198 model that includes transient defect reaction progress when  $t < t_{cr}$ . Henkes et al. (2014) state that  $G(t)$  follows a  
 199 first-order reaction (Eq. 9) with an apparent rate constant that evolves as (their Eq. A.11)

$$\kappa(t) = k_c + k_d e^{-k_2 t}. \quad (14)$$

200 Transient defects are assumed to react with rate  $k_d$  and anneal with time following a first-order reaction governed by  
 201  $k_2$  where  $k_2 \sim 1/t_{cr}$ . It can be seen from Eq. 14 that  $\kappa(t) = k_c$  when  $t \gg t_{cr}$ , as in the pseudo-first-order model above.

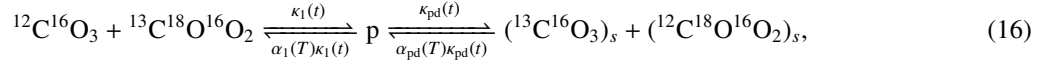
202 By comparing Eqs. 10 and 14, it is apparent that the transient defect/equilibrium defect model follows a parallel  
 203 superposition of first-order reactions with a distribution  $p(k)$  that satisfies

$$\frac{\int_0^{\infty} k p(k) e^{-kt} dk}{\int_0^{\infty} p(k) e^{-kt} dk} = k_c + k_d e^{-k_2 t}. \quad (15)$$

204 Finding  $p(k)$  involves solving the inverse Laplace transform, which in this case does not conform to a particular  
 205 function that can be derived analytically (see Section 3.2, below). Nonetheless, as an example, we show the  $p(k)$   
 206 distribution that satisfies Eq. 15 for optical calcite heated at 425 °C in Fig. S.1.

207 *3.1.3. Relationship to previous models: Stolper and Eiler (2015)*

208 Finally, we consider the "paired reaction-diffusion" model, which treats  $\Delta_{47}$  evolution as a serial reaction between  
 209 "clumps", "pairs", and "singletons". Equation 2 can be rewritten as



210 where p denotes "paired"  $^{13}\text{C}^{16}\text{O}_3$  groups immediately adjacent to  $^{12}\text{C}^{18}\text{O}^{16}\text{O}_2$  groups, the subscript "s" denotes  
 211 "singleton"  $^{13}\text{C}^{16}\text{O}_3$  or  $^{12}\text{C}^{18}\text{O}^{16}\text{O}_2$  groups that do not neighbor any other isotopically substituted group, and pd  
 212 denotes "pair diffusion" following Stolper and Eiler (2015) nomenclature. As in Stolper and Eiler (2015), we assume  
 213 each step of the reaction is described by a single unique rate constant  $\kappa_1(t) = k_1$  and  $\kappa_{\text{pd}}(t) = k_{\text{pd}}$  and equilibrium  
 214 constant  $\alpha_1(T)$  and  $\alpha_{\text{pd}}(T)$ . Equation 16 describes a system of paired first-order ordinary differential equations.

215 Two reactions occurring in series can be treated as a superposition of reactions occurring in parallel (Forney and  
 216 Rothman, 2014). Specifically for this system, we show in Appendix B that  $G(t)$  evolves as

$$G(t) = \sum_{i=1}^2 r(\lambda_i) e^{-\lambda_i t}, \quad (17)$$

217 where  $\lambda_i \propto k_1, k_{\text{pd}}$  are the eigenvalues of the reaction system and  $r(\lambda_i)$  represents  $p(k_i)$  projected onto its eigen-  
 218 vectors. The paired reaction-diffusion model is thus a specific case of disordered kinetics. Unlike  $p(k)$  however, in  
 219 general  $r(\lambda)$  need not be non-negative since eigenvectors can contain negative entries. Relaxing this constraint can  
 220 additionally explain non-monotonic  $G(t)$  evolution seen in aragonite heating experiments (Chen et al., 2019).

221 *3.1.4. Relaxing the non-negativity constraint*

222 It has recently been observed in isotopologue reordering experiments of aragonite that  $\Delta_{47}$  does not monotonically  
 223 approach  $\Delta_{47}^{\text{eq}}$  but rather increases transiently prior to decreasing (Chen et al., 2019). This was interpreted to reflect  
 224 an initial excess of pairs that rapidly back-react to form clumps on timescales shorter than that of singleton diffusion  
 225 [i.e., if  $\alpha_1(T)\kappa_1(t) \gtrsim \kappa_2(t)$ ]. This phenomenon is consistent with serial disordered reactions.

226 We show in Appendix C that, in general,

$$G(t) = \int_0^\infty r(\lambda) e^{-\lambda t} d\lambda, \quad (18)$$

227 which is the continuous version of Eq. 17 that allows  $\kappa_1(t)$  and  $\kappa_{\text{pd}}(t)$  to evolve with time. That is, we suppose that each  
 228 step in Eq. 16 is itself described by a superposition of first-order reactions that progress at different rates, consistent  
 229 with the assumption in Chen et al. (2019) that the activation energy of reaction between a given  $\text{CO}_3$  group and any  
 230 of its neighbors need not be identical. Again recognizing that  $r(\lambda)$  is a projection of  $p(k)$  onto the eigenvectors of the  
 231 reaction system, it follows that a  $r(\lambda)$  distribution containing significant negative area can lead to transient increases  
 232 in  $G(t)$  with time. We show a heuristic example of this phenomenon in Fig. S.2.

233 Negative  $r(\lambda)$  may be a general feature of serial and feedback systems in which some processes occur at much  
 234 faster rates than others. Negative  $r(\lambda)$  has also been observed in organic matter respiration experiments (Forney and

235 Rothman, 2014) and was interpreted to reflect a lag between serial reactions, analogous to the proposed time lag  
 236 between pair formation and singleton diffusion discussed in Stolper and Eiler (2015) and Chen et al. (2019).

237 Nonetheless, our current objective is to find the pdf of  $k$  that allows us to calculate the underlying activation energy  
 238 distribution and predict  $\Delta_{47}$  evolution over geologic timescales. We therefore omit aragonite experiments—which are  
 239 described by non-monotonic  $\Delta_{47}$  evolution—since negative  $r(\lambda)$  is inconsistent with a pdf (e.g., Eq. 7). Instead, we  
 240 proceed by finding the distribution of  $p(k)$  that best predicts observed  $G(t)$  evolution following Eq. 8 for apatite,  
 241 calcite, and dolomite heating experiments.

### 242 3.2. Fitting experimental data

243 Previous models derive rate equations after making assumptions about the system of reordering reactions; for  
 244 example, that transient defects anneal exponentially (Henkes et al., 2014) or that clumps react with pairs in series  
 245 (Stolper and Eiler, 2015). In effect, this prescribes the form of the  $p(k)$  distribution *a priori*. Here, we instead use an  
 246 inverse approach to find the  $p(k)$  distribution that best fits observed data without any *a priori* assumptions; we then  
 247 compare this solution to a theoretically justified pdf to estimate a functional form of  $p(k)$ .

#### 248 3.2.1. Finding the inverse solution

249 Since we expect  $k$  to vary over many orders of magnitude (Passey and Henkes, 2012; Henkes et al., 2014; Stolper  
 250 and Eiler, 2015; Brenner et al., 2018; Lloyd et al., 2018), we first perform a change of variables from  $k$  to  $\nu = \ln(k)$ .  
 251 This additionally facilitates the extraction of underlying activation energy distributions since  $E \propto \ln(k)$ . Probability is  
 252 conserved, so  $p(k)dk = \rho(\nu)d\nu$  and Eq. 8 becomes

$$G(t) = \int_{-\infty}^{\infty} \rho(\nu)e^{-e^{\nu}t}d\nu. \quad (19)$$

253 As shown in Appendix D, this can be written in matrix form as

$$\mathbf{G} = \mathbf{A}\boldsymbol{\rho}, \quad (20)$$

254 where  $\mathbf{G}$  is the length  $n_t$  vector of measured time-series  $G(t)$  values,  $\boldsymbol{\rho}$  is the length  $n_\nu$  vector of  $\rho(\nu)$  values, and  $\mathbf{A}$  is  
 255 the  $n_t \times n_\nu$  Laplace transform operator matrix. Although  $\boldsymbol{\rho}$  can be directly calculated as  $\boldsymbol{\rho} = \mathbf{A}^{-1}\mathbf{G}$ , this solution is  
 256 highly sensitive to noise at the level of  $\Delta_{47}$  analytical uncertainty and could lead to negative  $\rho(\nu)$  that is mathematically  
 257 possible but physically unreasonable (Forney and Rothman, 2012b; Hemingway et al., 2017). In mathematical terms,  
 258 Eq. 20 is ill posed (Hansen, 1994).

259 We thus use Tikhonov regularization to find the optimal solution that minimizes  $\rho(\nu)$  complexity (as determined  
 260 by the intensity of fluctuations; termed "roughness") while maximizing solution accuracy and ensuring that  $\rho(\nu) \geq 0$ .  
 261 Following Forney and Rothman (2012b), we calculate roughness as the  $n_\nu \times n_\nu$  bi-diagonal first-derivative operator  
 262 matrix,  $\mathbf{R}$  (Appendix D). The regularized inverse solution is found by including the roughness term in a constrained  
 263 least squares problem:

$$\min_{\boldsymbol{\rho}} \|\mathbf{G} - \mathbf{A}\boldsymbol{\rho}\| + \omega\|\mathbf{R}\boldsymbol{\rho}\| \quad (21)$$

264 subject to the constraints

$$\sum_{j=0}^{n_\nu} \rho_j = 1 \quad \text{and} \quad \rho_j \geq 0 \quad \text{for} \quad j = 1, \dots, n_\nu, \quad (22)$$

265 where  $\omega$  is a scalar that determines how much to weight roughness  $\|\mathbf{R}\boldsymbol{\rho}\|$  relative to residual error  $\|\mathbf{G} - \mathbf{A}\mathbf{x}\|$ . The  
266 optimal  $\omega$  is often taken as the point of maximum curvature in a log–log plot of residual error vs. roughness, where  
267 each point on the curve is calculated by solving Eq. 21 using  $\omega$  values that vary over many orders of magnitude (the  
268 so-called "L-curve"; Hansen, 1994). From this optimal point, increasing  $\omega$  greatly increases residual error but has  
269 little effect on solution roughness, whereas decreasing  $\omega$  greatly increases roughness but has little effect on residual  
270 error (e.g., Fig. 1A, D, G).

### 271 3.2.2. Finding the lognormal solution

272 For most samples, the regularized inverse distribution of  $\rho(\nu)$  resembles a Gaussian; that is,  $p(k)$  is approximately  
273 lognormally distributed (e.g., Fig. 1B, E, H). Lognormal  $p(k)$  distributions are theoretically justified since they derive  
274 naturally from the central limit theorem of multiplicative processes such as bond reordering (Montroll and Shlesinger,  
275 1982); they are commonly observed in disordered systems such as organic matter respiration (Forney and Rothman,  
276 2012a).

277 To compare with regularized inversion results, we determine the optimal lognormal distribution by setting  $\rho(\nu) \sim$   
278  $\mathcal{N}(\mu_\nu, \sigma_\nu)$  and finding the  $\mu_\nu$  and  $\sigma_\nu$  values that best reproduce observed data. That is, we solve

$$\min_{\mu_\nu, \sigma_\nu} \|\mathbf{G} - \mathbf{A}\boldsymbol{\rho}\|, \quad (23)$$

279 where each entry in  $\boldsymbol{\rho}$  is now subject to the constraint

$$\rho(\nu_i) = \frac{1}{\sqrt{2\pi}\sigma_\nu} e^{-(\nu_i - \mu_\nu)^2 / 2\sigma_\nu^2}, \quad i = 1, \dots, n_\nu. \quad (24)$$

280 For all isotopologue reordering experiments, optimal lognormal distributions give  $G(t)$  evolution estimates that are  
281 statistically indistinguishable from regularized inversion fits and are described by a root mean square error that is well  
282 within  $\Delta_{47}$  analytical uncertainty (e.g., Fig. 1C, F, I).

283 Furthermore, resulting lognormal distributions generally shift toward higher  $\mu_\nu$  and lower  $\sigma_\nu$  values with in-  
284 creasing experimental temperature (Fig. 2). Similar positive relationships between temperature and bond reordering  
285 reaction rates have been observed previously, thus motivating the use of an Arrhenius-like activation energy approach  
286 to determine bond reordering temperature dependence (Passey and Henkes, 2012; Henkes et al., 2014; Stolper and  
287 Eiler, 2015; Brenner et al., 2018; Lloyd et al., 2018).

### 288 3.3. Determining Activation Energies

289 Because our ultimate goal is to predict isotopologue reordering over geologic timescales, we extract the underlying  
290 reaction energetics to predict reaction rates at any arbitrary temperature. As in previous models (Passey and Henkes,

291 2012; Henkes et al., 2014; Stolper and Eiler, 2015), we suppose that each rate coefficient  $k$  follows the Arrhenius  
 292 equation

$$k(T) = k_0 e^{-E/RT}, \quad (25)$$

293 where  $T$  is temperature in Kelvin,  $k_0$  is the Arrhenius pre-exponential or "frequency" factor,  $E$  is the activation energy  
 294 of bond reordering for material associated  $k(T)$ , and  $R$  is the ideal gas constant. Treating  $k_0$  as constant is strictly  
 295 inconsistent with transition state theory of chemical reactions, which predicts  $k_0 \propto T$  (Eyring, 1935). However, linear  
 296 dependence of  $k_0$  on  $T$  only changes  $k$  by a factor of  $\sim 3$  over the temperature range of interest for isotopologue  
 297 reordering (i.e.,  $\sim 25 - 750$  °C), whereas the exponential term in Eq. 25 varies by many orders of magnitude over this  
 298 range. Thus, the assumption of constant  $k_0$  negligibly impacts resulting  $\Delta_{47}$  evolution predictions.

299 We seek  $p(E)$ , the pdf of  $E$  that leads to measured  $\rho(v)$  at a given  $T$ . If  $\rho(v) \sim \mathcal{N}(\mu_v, \sigma_v)$ , then we show in  
 300 Appendix E that  $p(E) \sim \mathcal{N}(\mu_E, \sigma_E)$  where

$$\begin{aligned} \mu_E &= RT(v_0 - \mu_v), \\ \sigma_E &= RT\sigma_v, \end{aligned} \quad (26)$$

301 and  $v_0 = \ln(k_0)$ . Rearranging yields

$$\begin{aligned} \mu_v &= v_0 - \frac{\mu_E}{R} \left( \frac{1}{T} \right), \\ \sigma_v &= \frac{\sigma_E}{R} \left( \frac{1}{T} \right). \end{aligned} \quad (27)$$

302 It can thus be seen from Eq. 27 that a Gaussian  $p(E)$  distribution leads to increasing  $\mu_v$  and decreasing  $\sigma_v$  with increas-  
 303 ing temperature, as is observed (Fig. 2). Similar to the approach taken in previous models (Passey and Henkes, 2012;  
 304 Henkes et al., 2014; Stolper and Eiler, 2015), we fit  $\rho(v)$  distributions to a suite of isothermal reordering experiments  
 305 performed at various temperatures and estimate  $\mu_E$  and  $\sigma_E$  by linearly regressing  $\mu_v$  and  $\sigma_v$  against  $1/T$  (Fig. 3).

### 306 3.4. Reordering on geologic timescales

307 Finally, we predict  $\Delta_{47}$  evolution over geologic timescales. This can be done analytically for the strictly heating  
 308 or cooling cases if  $d(T^{-1})/dt$  is constant (Dodson, 1973). However, we seek  $\Delta_{47}$  evolution for any arbitrary time-  
 309 temperature history. No analytical solution exists in this case since  $G(t)$  does not scale linearly with  $\Delta_{47}(t)$  and since  
 310  $G(t)$  need not decrease monotonically with  $t$  (Hemingway et al., 2017); put differently,  $\Delta_{47}(t)$  is free to increase  
 311 or decrease depending on the time-temperature history. We therefore numerically estimate  $\Delta_{47}(t)$  evolution for any  
 312 arbitrary time-temperature history following Passey and Henkes (2012). Rewriting Eqs. 5, 19, and 25 in discrete form  
 313 yields

$$\Delta_{47}(t_i) = \Delta_{47}^{\text{eq}}(T_i) + \left[ \Delta_{47}(t_{i-1}) - \Delta_{47}^{\text{eq}}(T_i) \right] \Delta G_i, \quad (28)$$

314 where

$$\begin{aligned} \Delta G_i &= \left[ \sum_{j=1}^{n_E} \mathcal{N}(\mu_E, \sigma_E) \exp \left( - \exp \left[ \nu_0 - \frac{E_j}{RT(t_i)} \right] \Delta t \right) \Delta E \right], \\ i &= 2, \dots, n_t, \\ j &= 1, \dots, n_E, \end{aligned} \quad (29)$$

315  $\Delta t$  and  $\Delta E$  are the discrete  $t$  and  $E$  steps, and we impose the initial condition  $\Delta_{47}(t_1) = \Delta_{47}^0$ . This is written in matrix  
316 form as

$$\begin{aligned} \Delta_{47} &= \phi(\mathbf{t}, \mathbf{T}|\mathbf{y}), \\ \mathbf{y} &= \left[ \Delta_{47}^0, \mu_E, \sigma_E, \nu_0 \right], \end{aligned} \quad (30)$$

317 where  $\mathbf{t}$  and  $\mathbf{T}$  are the length  $n_t$  discretized time and temperature vectors,  $\phi$  denotes the function described in Eqs.  
318 28–29 solved at each  $t_i$ ,  $T_i$  given the input parameter values in  $\mathbf{y}$ , and  $\Delta_{47}$  is the length  $n_t$  vector of resulting  $\Delta_{47}$   
319 values.

320 We additionally propagate  $\Delta_{47}$  uncertainty. Uncertainty is derived from each input parameter in  $\mathbf{y}$ , which contains  
321 either analytical error (for  $\Delta_{47}^0$ ) or regression error associated with each Arrhenius plot (for  $\mu_E$ ,  $\sigma_E$ , and  $\nu_0$ ; Fig. 3).  
322 We implicitly assume  $\Delta_{47}^{\text{eq}}(T_i)$  is perfectly known for all  $T_i$ . This assumption is not strictly true; however,  $\Delta_{47}^{\text{eq}}(T)$  error  
323 is expected to be minor relative to that of each parameter in  $\mathbf{y}$  given the strong correlation and low uncertainty in  $T$   
324 vs.  $\Delta_{47}^{\text{eq}}(T)$  calibration equations (Schauble et al., 2006; Passey and Henkes, 2012; Bonifacie et al., 2017; Lloyd et al.,  
325 2018).

326 Some input parameters are highly correlated—in particular,  $\nu_0$  and  $\mu_E$  (Fig. 3). We account for covariance by  
327 propagating error using a Taylor expansion approach (Ku, 1966). Specifically, we calculate  $\Delta_{47}$  variance at each  $t_i$  as

$$\Sigma_{\Delta_{47}\Delta_{47}} = \mathbf{J}\Sigma_{\mathbf{y}\mathbf{y}}\mathbf{J}^T, \quad (31)$$

328 where  $\mathbf{J}$  is the  $n_t \times 4$  Jacobian matrix of  $\phi(\mathbf{t}, \mathbf{T}|\mathbf{y})$ ,  $\Sigma_{\mathbf{y}\mathbf{y}}$  is the  $4 \times 4$  covariance matrix of  $\mathbf{y}$ , and  $\Sigma_{\Delta_{47}\Delta_{47}}$  is the resulting  
329  $n_t \times n_t$  covariance matrix of predicted  $\Delta_{47}$  values. The  $\pm 1\sigma$  uncertainty in predicted  $\Delta_{47}$  values is readily determined  
330 as  $\sqrt{\text{diag}(\Sigma_{\Delta_{47}\Delta_{47}})}$ .

## 331 4. Results

### 332 4.1. Inverse and lognormal rate distributions

333 Most regularized inverse  $\rho(\nu)$  distributions are unimodal, symmetric, and lead to predicted  $G(t)$  evolution with a  
334 model-data misfit—determined by the root mean square error (rmse)—that is comparable to analytical uncertainty  
335 (Fig. 1, 2; Table S.3). Still, there exist two exceptions to this behavior: First, low-temperature experiments ( $\lesssim 350$  °C)  
336 can result in broad, left-skewed  $\rho(\nu)$  distributions (e.g., Fig. 1B); this is most apparent for experiments exhibiting small  
337 signals and thus analytical signal-to-noise ratios of  $\lesssim 5$ . In extreme cases, left-skewed  $\rho(\nu)$  distributions can extend

338 to  $\nu \ll -40$ , equivalent to rates of  $\ll e^{-40} \text{ min}^{-1}$  at these experimental conditions (Fig. S.3). Material associated  
339 with such slow rates would exhibit bond reordering residence times of  $\gg 10^{11}$  years and thus remains unreacted  
340 over experimental timescales. Second, very high-temperature experiments ( $\gtrsim 500 \text{ }^\circ\text{C}$ ) can lead to right-skewed  $\rho(\nu)$   
341 distributions (e.g., Fig. 1H) that extend to  $\nu \gg 10$ , equivalent to rates of  $\gg e^{10} \text{ min}^{-1}$ . Material associated with such  
342 fast rates would exhibit bond reordering residence times of  $\ll 10^{-5}$  seconds, orders of magnitude shorter than the  
343 duration between any two experimental time points and thus not resolvable in any existing dataset.

344 Both left- and right-skew behaviors are mathematically feasible but physically unconstrained; they emerge when  
345 some fraction of material is associated with rates that lead to bond reordering on timescales that lie significantly  
346 outside of the analytical time window. We therefore omit from further consideration low-temperature experiments  
347 with signal-to-noise  $\leq 5$  ( $n = 4$ ) as well as high-temperature experiments that reach their  $\Delta_{47}^{\text{eq}}(T)$  value prior to the first  
348 experimental measurement ( $n = 2$ ), although this choice does not exert a major impact on observed trends. Our final  
349 data set includes 24 calcite experiments (spanning 4 studies, 6 calcite types, and 2 pressure/hydration conditions), 1  
350 apatite experiment, and 4 dolomite experiments. Regularized inverse  $\rho(\nu)$  distributions of retained experiments exhibit  
351 a  $\log_{10}$  rmse averaging  $-2.18 \pm 0.22 \text{ } \%$ , a  $\log_{10}$  roughness averaging  $-2.65 \pm 0.43$ , and a  $\log_{10} \omega$  averaging  $0.08 \pm 0.54$   
352 (mean  $\pm$  stdev.;  $n = 29$ ); this rmse is comparable to the typical analytical uncertainty of  $\sim 0.01 \text{ } \%$  CDES<sub>90</sub> (Table S.2),  
353 as expected (Forney and Rothman, 2012b).

354 Lognormal  $\rho(\nu)$  distributions exhibit an average  $\log_{10}$  rmse of  $-2.08 \pm 0.21 \text{ } \%$  (mean  $\pm$  stdev.;  $n = 29$ ) and  
355 typically result in  $G(t)$  evolutions that are nearly identical to those predicted by regularized inverse solutions (Fig. 1).  
356 This similarity holds even for experiments exhibiting left- or right-skewed inverse solutions since any  $G(t)$  evolution  
357 differences resulting from such skew will only manifest outside of the analytical time window. For the entire dataset,  
358  $\mu(\nu)$  averages  $-5.91 \pm 3.25 \ln(\text{min}^{-1})$  and exhibits a strong positive correlation with temperature whereas  $\sigma(\nu)$  averages  
359  $2.93 \pm 1.01 \ln(\text{min}^{-1})$  and exhibits a strong negative correlation with temperature (Fig. 2-3). Propagated model fit  
360 uncertainty is small, with error in estimated parameters averaging  $\pm 0.35 \ln(\text{min}^{-1})$  for  $\mu(\nu)$  and  $\pm 0.45 \ln(\text{min}^{-1})$  for  
361  $\sigma(\nu)$ .

#### 362 4.2. Comparison to previous models

363 The lognormal distributed kinetic model developed here results in model fits that are comparable to or better than  
364 those for both the transient defect/equilibrium model (Henkes et al., 2014) and the paired reaction-diffusion model  
365 (Stolper and Eiler, 2015). All models provide similar model-data misfit rmse values. However, estimated  $\mu(\nu)$  and  
366  $\sigma(\nu)$  uncertainty is considerably less than that predicted for Henkes et al. (2014) and Stolper and Eiler (2015) model  
367 parameters, leading to smaller propagated error in  $G(t)$  evolution predictions (Fig. 4A).

368 Furthermore, treating reordering rates as a continuous distribution naturally leads to a gradual slowdown in  $G(t)$   
369 evolution with time; in contrast, the "kinked" rate slowdown behavior of previous models results from fitting a finite  
370 set of discrete rates to each experiment (3 for the transient defect/equilibrium defect model; 2 for the paired reaction-  
371 diffusion model). This difference in gradual vs. kinked rate slowdown leads to slightly divergent model behavior,

372 evidenced by the differences in predicted – measured  $\Delta_{47}$  evolution between different model types (Fig. 4B). Specifi-  
 373 cally, both the transient defect/equilibrium defect and the paired reaction-diffusion models tend to over-predict  $\Delta_{47}$  at  
 374 intermediate time points and under-predict  $\Delta_{47}$  at late time points; in contrast, the lognormal distributed kinetic model  
 375 exhibits either the opposite behavior or no trend with time. Although these differences are small and statistically in-  
 376 significant over the timescales of heating experiments considered here, they may become significant if projected over  
 377 longer experimental timescales.

Table 1: Arrhenius regression activation energy distribution results (Eq. 27) for individual calcite and dolomite sample materials and for the "all calcite" average. Experiments exhibiting noisy data [i.e.,  $\Delta_{47}(t)$  signal-to-noise < 5] or non-monotonic  $\Delta_{47}(t)$  evolution were excluded from these calculations (see Sec. 4.3 and Table S.3). Sample materials are only included here if  $\geq 3$  experiments were retained after this screening procedure. OC = optical calcite; BC = brachiopod shell calcite; SC = spar calcite; D = dolomite; WHP = wet, high-pressure experiments;  $n$  = number of experiments included in Arrhenius regression.

sample	$\mu_E$ (kJ mol <sup>-1</sup> )		$\nu_0$ (min <sup>-1</sup> )		$\sigma_E$ (kJ mol <sup>-1</sup> )		$n$	data reference
	mean	std. dev.	mean	std. dev.	mean	std. dev.		
Eugui dolomite (D)	230.3	47.7	29.0	6.8	14.8	2.2	4	Lloyd et al. (2018)
MGB-CC-1 (OC)	290.2	27.1	42.7	4.6	20.4	1.8	5	Passey and Henkes (2012)
MGB-CC-1 (OC; WHP)	277.8	40.9	41.2	7.1	13.5	2.7	4	Brenner et al. (2018)
NE-CC-1 (SC)	264.4	16.8	35.6	2.7	24.3	0.8	6	Passey and Henkes (2012)
Mexico calcite (OC)	250.7	13.6	34.2	2.3	15.7	1.7	3	Stolper and Eiler (2015)
WA-CB-13 (BC)	247.4	15.6	35.8	2.6	16.6	0.6	5	Henkes et al. (2014)
<b>All calcite average</b>	<b>224.3</b>	<b>27.6</b>	<b>31.5</b>	<b>4.6</b>	<b>17.4</b>	<b>0.7</b>	<b>24</b>	–

### 378 4.3. Activation energy distributions

379 Similar to previous observations, disordered kinetic model parameter values scale linearly with  $1/T$  following  
 380 Arrhenius-like behavior (Fig. 3). Combining all calcite samples yields a  $\mu_\nu$  Arrhenius regression described by  $\mu_E =$   
 381  $224.3 \pm 27.6$  kJ mol<sup>-1</sup> and  $\nu_0 = 31.5 \pm 4.6$  ln(min<sup>-1</sup>) and a  $\sigma_\nu$  Arrhenius regression described by  $\sigma_E = 17.4 \pm 0.7$   
 382 kJ mol<sup>-1</sup> [ $\mu_\nu$  rmse = 1.3 ln(min<sup>-1</sup>);  $\sigma_\nu$  rmse = 0.9 ln(min<sup>-1</sup>);  $n = 24$ ]. Similarly, dolomite experiments yield a  $\mu_\nu$   
 383 Arrhenius regression described by  $\mu_E = 230.3 \pm 47.7$  kJ mol<sup>-1</sup> and  $\nu_0 = 29.0 \pm 6.8$  ln(min<sup>-1</sup>) and a  $\sigma_\nu$  Arrhenius  
 384 regression described by  $\sigma_E = 14.8 \pm 2.2$  kJ mol<sup>-1</sup> [ $\mu_\nu$  rmse = 0.5 ln(min<sup>-1</sup>);  $\sigma_\nu$  rmse = 0.6 ln(min<sup>-1</sup>);  $n = 4$ ].

385 When separated into individual experimental materials, calculated  $\mu_E$  ranges from a minimum of  $230.3 \pm 47.7$   
 386 kJ mol<sup>-1</sup> for Eugui dolomite to a maximum of  $290.2 \pm 27.1$  kJ mol<sup>-1</sup> for optical calcite sample MGB-CC-1; similarly,  
 387  $\sigma_E$  ranges from a minimum of  $14.8 \pm 2.2$  kJ mol<sup>-1</sup> for Eugui dolomite to a maximum of  $24.3 \pm 0.8$  kJ mol<sup>-1</sup> for spar  
 388 calcite sample NE-CC-1 (Table 1). Although all calculated  $\mu_E$  results are statistically identical (two-tailed  $t$  test;  
 389  $p > 0.05$ ), the "combined calcite" value appears lower than that for any individual calcite type due to bias caused by

390 differences in the  $1/T$  ranges spanned by experiments using different calcite types. In contrast to  $\mu_E$ , calculated  $\sigma_E$   
391 values can exhibit statistically significant differences between sample materials ( $p < 0.05$ ; Table 1), potentially due  
392 to differences in trace element contents, ionic impurities, and/or crystallographic defect concentrations (Henkes et al.,  
393 2014; Lloyd et al., 2018).

394 Arrhenius regression results exhibit a minor dependence on the choice of  $\Delta_{47}^{\text{eq}}(T)$  calibration equation (Bonifacie  
395 et al., 2017; Lloyd et al., 2018). Specifically, recalculating lognormal disordered kinetic model fits and Arrhenius re-  
396 gression parameters using the  $\Delta_{47}^{\text{eq}}(T)$  equation advocated by Lloyd et al. (2018) (their Eq. 4) decreases the "combined  
397 calcite"  $\mu_E$  value to  $205.5 \pm 31.1 \text{ kJ mol}^{-1}$  and leads to slightly higher rmse values but has little impact on  $\nu_0$  and  
398  $\sigma_E$  [ $\mu_\nu$  rmse =  $1.4 \ln(\text{min}^{-1})$ ;  $\sigma_\nu$  rmse =  $1.5 \ln(\text{min}^{-1})$ ;  $n = 24$ ; Fig. S.4]. In contrast, recalculating dolomite results  
399 using the Lloyd et al. (2018)  $\Delta_{47}^{\text{eq}}(T)$  equation increases  $\mu_E$  to  $258.3 \pm 43.7 \text{ kJ mol}^{-1}$  and  $\sigma_E$  to  $20.9 \pm 3.4 \text{ kJ mol}^{-1}$   
400 [ $\mu_\nu$  rmse =  $0.5 \ln(\text{min}^{-1})$ ;  $\sigma_\nu$  rmse =  $0.8 \ln(\text{min}^{-1})$ ;  $n = 4$ ; Fig. S.4]. Still, none of these differences in Arrhenius  
401 parameters calculated using the Bonifacie et al. (2017) or the Lloyd et al. (2018)  $\Delta_{47}^{\text{eq}}(T)$  calibration equations is sta-  
402 tistically significant (two-tailed  $t$  test;  $p > 0.05$ ). In principle, this conclusion should apply for other clumped isotope  
403 temperature calibrations, although few span as wide a temperature range or include as many mineralogies as Bonifacie  
404 et al. (2017).

## 405 5. Discussion

### 406 5.1. Model results, implication, and application

407 This disordered kinetic model provides a generalizable framework of carbonate isotopologue bond reordering. Im-  
408 portantly, previous models of this phenomenon (Henkes et al., 2014; Stolper and Eiler, 2015)—developed to describe  
409 early, fast  $\Delta_{47}$  changes observed in laboratory heating experiments—can be treated as specific cases of disordered  
410 kinetics.

411 By extracting the underlying activation energy distributions using an Arrhenius parameterization (Fig. 3), this  
412 approach may help predict bond reordering in future experiments using either previously studied minerals (i.e., calcite  
413 and dolomite) or other carbonates (e.g., siderite and magnesite). The finding that  $\mu_E$  for the "all calcite average"  
414 is lower than  $\mu_E$  for dolomite is consistent with the conclusions of Lloyd et al. (2018) (their Fig. 5) and implies  
415 that observed differences between calcite and dolomite from the same metamorphic system are driven, at least in  
416 part, by differential isotopologue reordering behavior during the same thermal history. Unfortunately, there were  
417 not enough heating experiments on carbonate groups in apatite that met our screening criteria to derive  $\mu_E$  and  $\sigma_E$   
418 values (see Sec. 4.1). We nonetheless find that apatite  $\mu_\nu$  is lower than calcite but identical to dolomite at equivalent  
419 experimental temperatures, whereas apatite  $\sigma_\nu$  appears to be slightly lower than any observed calcite or dolomite  
420 value (Fig. 3). This result is consistent with original conclusions of Stolper and Eiler (2015) but conflicts with their  
421 carbonatite data indicating apatite exhibits lower apparent equilibrium temperatures than does calcite. More apatite

422 heating experiments are thus warranted to further refine these mineralogical differences and to test the hypothesis that  
423 dolomite and apatite exhibit similar, if not identical, isotopologue reordering kinetics.

424 Insight into relative bond reordering rates may also come from studies of geologic settings containing different  
425 carbonate mineralogies that have experienced the same, elevated thermal history; for example, metamorphic systems,  
426 deeply buried sedimentary carbonates, and complex carbonatites. Indeed, observations from such settings formed the  
427 original motivation for previous bond reordering models, since these scenarios are thought to reflect reordering over  
428 geologic timescales.

429 Future studies that include independently constrained thermal histories will provide important natural tests of  
430 laboratory-derived kinetics. For example,  $\Delta_{47}$  measurements on carbonatites result in  $T(\Delta_{47})$  values far below the  
431 canonically known temperatures of crystallization (Dennis and Schrag, 2010). Akin to the concept of closure tempera-  
432 ture in thermochronology (Dodson, 1973), this so-called "apparent equilibrium"  $\Delta_{47}$ -derived temperature, or  $T(\Delta_{47})_{ae}$ ,  
433 has been shown to depend on geologic cooling rate (Passey and Henkes, 2012). While  $T(\Delta_{47})_{ae}$  measurements may  
434 provide a useful geospeedometer, cooling rate predictions are currently somewhat sensitive to the choice of bond re-  
435 ordering kinetic model (Fig. 5A). All models predict similar  $T(\Delta_{47})_{ae}$  values of  $\approx 100$  to  $200$  °C for geologic cooling  
436 rates between  $10^{-8}$  and  $10^{-4}$  °C yr<sup>-1</sup>, broadly consistent with published  $\Delta_{47}$  measurements of carbonatites and marbles  
437 (Dennis and Schrag, 2010; Stolper and Eiler, 2015; Lloyd et al., 2017). Interestingly, this similarity at slow cooling  
438 rates includes both dolomite and calcite predictions. However,  $T(\Delta_{47})_{ae}$  values diverge significantly at faster rates.  
439 For a given mineral, the disordered kinetic model presented here always predicts lower  $T(\Delta_{47})_{ae}$  values than both pre-  
440 vious models—although these differences are not statistically significant at the slowest cooling rates—and suggests  
441 that calcite  $T(\Delta_{47})_{ae} \gtrsim 400$  °C as the result of isotopologue reordering in natural samples at geologically reasonable  
442 cooling rates should be rare.

443 The  $\Delta_{47}$  preservation of low-temperature carbonates such as shells, micritic cements, and carbonate nodules can  
444 similarly be evaluated in the context of isotopologue reordering (Henkes et al., 2014, 2018). Such materials have been  
445 shown to exhibit high  $T(\Delta_{47})$  values without any obvious geochemical alteration to the original mineral (Henkes et al.,  
446 2014; Stolper and Eiler, 2015); understanding this phenomenon is critical for screening and omitting altered samples  
447 from paleoclimate studies (e.g., Henkes et al., 2018). However, the time-temperature history at which reordering is  
448 predicted to occur again depends somewhat on the choice of kinetic model (Fig. 5B). Specifically, the model presented  
449 here conforms to previous, canonical limits of  $\Delta_{47}$  preservation, but results in a left-ward shift for both "incipient"  
450 (1%) and "complete" (99%) reordering curves. That is, relative to previous models, ours predicts that less time and/or  
451 lower temperatures are needed to reach the same degree of alteration and suggests that previous models overestimate  
452 the temperatures at which isotopologue reordering is activated. Observed differences between models may be driven  
453 in part by our use of a single calcite Arrhenius regression (Fig. 3) rather than sample-specific (e.g., brachiopod fossil  
454 in Henkes et al., 2014) or experiment-specific curves (e.g., hydrothermal reactions in Brenner et al., 2018). When  
455 separated by calcite type, our model conforms more closely to predictions of Henkes et al. (2014), particularly for  
456 brachiopod shell materials (Fig. S.5).

## 457 5.2. Geologic tests

458 We consider two hypothetical thermal histories where the predictions of the calcite kinetic model presented here  
459 might be applied in practice. There are few, if any, natural systems where a complete thermal history of a carbonate  
460 rock is known independently (e.g., from thermochronology) and where  $\Delta_{47}$  has been measured on a sufficient number  
461 of samples for a detailed evaluation of measured vs. predicted results (but see Shenton et al., 2015; Lloyd et al.,  
462 2017; Lawson et al., 2018, for recent attempts). Here, we instead compare model performance under two hypothetical  
463 but geologically reasonable scenarios: (i) a rock that was heated in excess of laboratory experimental temperatures  
464 ( $>500^\circ\text{C}$ ) and then cooled by conduction over  $\sim 10^7$  yr (Fig. 6A) and (ii) a sedimentary carbonate buried to depths of  
465 several kilometers in a late Paleozoic foreland basin (Fig. 6C).

466 In the first scenario, we define the thermal history by a 1D thermal diffusion model whereby an intrusion cools by  
467 contact with the country rock (adapted from Ehlers, 2005). Such a simple cooling history could represent a number  
468 of geologic settings, including contact metamorphism (Lloyd et al., 2017), carbonate sedimentary rock adjacent to a  
469 dike (Finnegan et al., 2011), or other extreme rapid heating and cooling processes. As observed by Passey and Henkes  
470 (2012), carbonate clumped isotopes behave much like a thermochronometer in this scenario; the rate of cooling  
471 determines the final  $\Delta_{47}$  value (Fig. 5A). Here, we set the model for a  $550^\circ\text{C}$  intrusion 3 km in diameter that cools  
472 by thermal diffusion with  $30^\circ\text{C}$  country rock with a diffusivity of  $30\text{ km}^2\text{ Ma}^{-1}$ . Given that the starting temperature  
473 is equivalent to the warmest laboratory heating experiments (i.e., isotopologue reordering within minutes), all kinetic  
474 models predict apparent equilibrium temperature behavior. However, each model results in a different  $T(\Delta_{47})_{\text{ae}}$  value  
475 (Fig. 6B). The calcite lognormal disordered kinetic model predicts a lower  $T(\Delta_{47})_{\text{ae}}$  and a shorter interval of departure  
476 from equilibrium than both the Henkes et al. (2014) and Stolper and Eiler (2015) models, suggesting  $\Delta_{47}$  systematics  
477 are more "open" during the cooling of igneous and metamorphic rocks than previously thought. This difference could  
478 be tested empirically in simple, natural systems where cooling rates are constrained either by thermochronometry or  
479 robust geophysical models. Furthermore, predicted dolomite  $T(\Delta_{47})_{\text{ae}}$  is  $\approx 70^\circ\text{C}$  higher than for calcite, as expected  
480 (Fig. 5A), although overlapping error bars should motivate future refinement of dolomite kinetics.

481 The second scenario approaches isotopologue bond reordering temperatures over  $\sim 10^6$  to  $10^7$  yr timescales (Fig.  
482 6C, D) and is relevant to much of the Phanerozoic rock record. To mimic warm, deep histories that typify Paleozoic  
483 and early Mesozoic rocks—and thus represent burial temperatures high enough to activate bond reordering—we base  
484 the shape of this burial history curve on Late Paleozoic sediments exposed in the Arrow Canyon Range, eastern  
485 Great Basin province, NV, USA (Shenton et al., 2015). Unlike the conductive cooling case described above, modeled  
486  $T(\Delta_{47})$  exhibits complex and varied features (Fig. 6D). Specifically, the disordered kinetic model for calcite predicts an  
487 incipient  $T(\Delta_{47})$  response to increasing burial temperatures at  $\approx 100^\circ\text{C}$ , consistent with the canonical preservation limit  
488 for  $\Delta_{47}$  over  $10^7$  to  $10^8$  yr timescales (Fig. 5) and similar to that predicted by Stolper and Eiler (2015) but cooler than  
489 predicted by Henkes et al. (2014). Interestingly, our model then predicts a rapid approach to equilibrium at elevated  
490 burial temperatures; this leads to closure temperature-like behavior and a final  $T(\Delta_{47})_{\text{ae}}$  that is intermediate between  
491 that predicted by Henkes et al. (2014)—which only reaches equilibrium at the highest modeled burial temperature—

492 and by Stolper and Eiler (2015)—which never reaches equilibrium. Dolomite behavior is similar to that of calcite  
493 predicted by Henkes et al. (2014), with nearly identical predicted final  $T(\Delta_{47})_{ac}$  values. Alternative sediment burial  
494 histories with less dwell time in the "completely reordered" region of Fig. 5B will yield trajectories where  $T(\Delta_{47})$   
495 infrequently reaches model  $T$ .

### 496 5.3. Outlook

497 The adaptation of disordered kinetic models to describe internal isotopologue reordering in carbonates will enable  
498 more targeted future experiments and will provide more robust predictions of bond reordering when applied to natural  
499 systems. For example, new high-temperature  $\mu_v$  and  $\sigma_v$  observations for calcite and dolomite—as well as additional  
500 observations for apatite carbonate groups—will further refine the activation energy distributions predicted here. More  
501 generally, it has been suggested that various carbonate minerals may be described by unique isotopologue reordering  
502 activation energy distributions, possibly driven by inherent differences in metal-oxide bond strength (Lloyd et al.,  
503 2018). Accurately constraining these distributions may allow for the derivation of independent cooling rates from  
504 the same rock in geologic systems that contain multiple carbonate types (Ryb et al., 2017; Lloyd et al., 2017). Such  
505 a mineralogical driver of isotopologue reordering kinetics would predict that one mineralogy can be thermally reset  
506 while another, more refractory carbonate may preserve its formation  $\Delta_{47}$  values after experiencing the same thermal  
507 history. Additionally, it has been observed that the same carbonate mineralogy (i.e., calcite) may record different  $\Delta_{47}$   
508 signatures after burial (Shenton et al., 2015). While the underlying reason(s) for this phenomenon remain elusive,  
509 improvements in error propagation developed here (e.g., Fig. 6D) can provide an empirical means to interrogate such  
510 trends.

511 This disordered kinetic framework can be adapted to characterize the reordering kinetics of other, novel mineral  
512 isotopologue measurements. For example, sulfate, phosphate, and silicates all contain isotopologue arrangements that  
513 include clumps analogous to  $^{13}\text{C}-^{18}\text{O}$  (e.g.,  $^{34}\text{S}-^{18}\text{O}$ ) and/or double heavy isotope substitutions (e.g.,  $^{18}\text{O}-^{18}\text{O}$ ) in the  
514 oxyanion group; these minerals are likely subject to analogous diffusive bond rearrangement at elevated temperatures  
515 over geologic timescales. Measurement of such isotopologues with sufficient precision to resolve both natural and  
516 experimentally induced isotope effects is imminent (Ueno et al., 2019; Neubauer et al., 2020). Furthermore, future  
517 carbonate heating experiments should additionally target  $^{12}\text{C}^{16}\text{O}^{18}\text{O}_2$  isotopologue evolution (i.e.,  $\Delta_{48}$ ) as a complemen-  
518 tary isotopic marker for diffusive C–O bond breakage and reformation in the solid mineral lattice. Although analytical  
519 signal-to-noise may render  $\Delta_{48}$  experiments somewhat limited (Fiebig et al., 2019), the development of a disordered  
520 kinetic framework for multiple isotopologue bond reordering should nonetheless be trivial (Section 3.1). Finally, a  
521 disordered kinetic approach may be usefully applied to mineral-pair isotope exchange kinetics and systems where the  
522 same elements occupies different intercrystalline sites (e.g., oxyhydroxides; Miller et al., 2020). Laboratory isotope  
523 studies may also be combined with high-resolution spectroscopy, X-ray diffraction, or NMR to further elucidate the  
524 crystalline environment that underpins this diffusive elemental exchange (e.g., Chen et al., 2019).

## 525 6. Conclusion

526 Here, we derive a disordered kinetic model for carbonate clumped isotope bond reordering that accurately charac-  
527 terizes early, rapid changes in  $\Delta_{47}$  observed during calcite, dolomite, and apatite laboratory heating experiments. This  
528 framework can be extended to describe  $\Delta_{47}$  evolution other minerals, including non-monotonic aragonite evolution  
529 (Chen et al., 2019). Importantly, we show theoretically that two previous models—the transient defect/equilibrium  
530 defect model (Sec. 3.1.2; Henkes et al., 2014) and the paired reaction-diffusion model (Sec. 3.1.3; Stolper and Eiler,  
531 2015)—represent specific cases of disordered kinetics. By fitting published heating experiment  $\Delta_{47}$  data using an in-  
532 verse approach, we show that isotopologue reordering rate distributions are approximately lognormal, consistent with  
533 the central limit theorem. To allow for the extrapolation of reordering kinetic model results to geologic scenarios, we  
534 then determine the underlying Gaussian activation energy distributions using an Arrhenius approach.

535 We additionally consider isotopologue reordering model performance for a range of hypothetical geologic scenar-  
536 ios. Generally, our model does not make major revisions to the predictions of previous models. Over geologically  
537 reasonable linear cooling rates, all isotopologue reordering models result in  $T(\Delta_{47})_{ae} < 600$  °C, with our model  
538 suggesting that observed  $T(\Delta_{47})_{ae} > 400$  °C should be rare for calcite. We also suggest that previous models over-  
539 estimated the  $\Delta_{47}$  preservation threshold for calcite paleotemperature archives (e.g., fossil shells). These differences  
540 are minor for incipient isotopologue reordering, which conforms with canonical limits established by Henkes et al.  
541 (2014), but are larger for nearly complete resetting of  $\Delta_{47}$ . For more complex thermal histories, which are relevant to  
542 metamorphic and sedimentary carbonates, we show that the disordered kinetic model yields reductions in error that  
543 will be important for empirical tests of model predictions. Disordered kinetics should also be amenable to  $\Delta_{47}$  heating  
544 experiments that mimic geologic cooling, whereby a carbonate is heated to elevated temperatures and cooled over  
545 laboratory timescales. Lastly, we hypothesize that framework should be easily adapted to other current and future  
546 mineral isotopologue measurements such as carbonate  $^{18}\text{O}$ – $^{18}\text{O}$  ( $\Delta_{48}$ ) and sulfate  $^{34}\text{S}$ – $^{18}\text{O}$ .

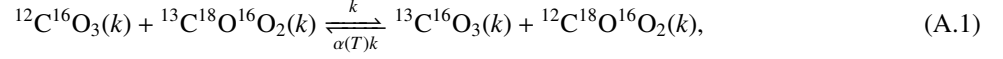
547 Accompanying this paper is an open-source Python package 'isotopylog' (Hemingway, 2020) that allows for  
548 model comparisons, incorporation of new isotopologue reordering experiment data (including from new carbonate  
549 mineralogies), and the prediction of  $\Delta_{47}$  during any point of a geologic thermal history.

## 550 Acknowledgements

551 We thank David Johnston, Alison Piasecki, and Mark Brandon for helpful discussions; Daniel Stolper for consul-  
552 tation on the paired diffusion model implementation; and the organizers of the Banff Geobiology Society Conference  
553 2019 for stimulating our initial collaborations on this topic. J.D.H. was supported by an NSF Early-Concept Grant for  
554 Exploratory Research (EAGER) number EAR1839341 and an American Chemical Society Petroleum Research Fund  
555 Grant number 59455-ND2.

556 **Appendix A. Deriving the first-order rate equation**

557 The carbonate isotopologue reordering reaction for material associated with a given rate constant  $k$  in a closed  
558 system can be written as



559 where we have appended each species with  $(k)$  to emphasize that this reaction only describes the subset of material  
560 associated with rate  $k$ . In all subsequent equations, we replace each species with its atomic mass for convenience.  
561 This implicitly ignores contributions to each atomic mass by  $^{17}\text{O}$ -containing isotopologues since these are negligible  
562 (Wang et al., 2004; Schauble et al., 2006). Following Eq. A.1, the derivative of  $^{13}\text{C}^{18}\text{O}^{16}\text{O}_2$  abundance with respect  
563 to time can be written as

$$\frac{d[63](k, t)}{dt} = -k[63](k, t)[60](k, t) + \alpha(T)k[61](k, t)[62](k, t), \quad (\text{A.2})$$

564 where  $[i]$  denotes the fractional abundance of atomic mass  $i$  such that  $\sum_{i=60}^{63}[i] = 1$  (ignoring negligible contributions  
565 by other multiply substituted isotopologues; Passey and Henkes, 2012). Similarly following Eq. A.1, we have

$$\alpha(T) = \frac{[60]_{\text{eq}}[63]_{\text{eq}}}{[61]_{\text{eq}}[62]_{\text{eq}}}, \quad (\text{A.3})$$

566 where the subscript "eq" denotes equilibrium abundance at temperature  $T$ ; importantly, equilibrium abundances are in-  
567 dependent of  $k$ . Because  $^{12}\text{C}^{16}\text{O}_3$ ,  $^{13}\text{C}^{16}\text{O}_3$  and  $^{12}\text{C}^{18}\text{O}^{16}\text{O}_2$  are orders-of-magnitude more abundant than  $^{13}\text{C}^{18}\text{O}^{16}\text{O}_2$   
568 (Wang et al., 2004; Affek and Eiler, 2006), we assume that changes in the concentrations of these species are negligible  
569 and let

$$\begin{aligned} [60](k, t) &= [60]_{\text{eq}}, \\ [61](k, t) &= [61]_{\text{eq}}, \\ [62](k, t) &= [62]_{\text{eq}}. \end{aligned} \quad (\text{A.4})$$

570 Combining Eqs. A.2–A.4 yields

$$\frac{d[63](k, t)}{dt} = -k[60]_{\text{eq}} \{ [63](k, t) - [63]_{\text{eq}} \}, \quad (\text{A.5})$$

571 which is a separable first-order differential equation of the form  $x'(t) = a[x(t) + b]$ . Because  $[60]_{\text{eq}} \approx 1$  (Wang et al.,  
572 2004; Affek and Eiler, 2006), we subsume this term into  $k$ . The fractional abundance of  $^{13}\text{C}^{18}\text{O}^{16}\text{O}_2$  at time  $t$  can thus  
573 be determined by integrating Eq. A.5 from an initial time  $t = 0$ :

$$\frac{[63](k, t) - [63]_{\text{eq}}}{[63]_0 - [63]_{\text{eq}}} = e^{-kt}, \quad (\text{A.6})$$

574 where  $[63]_0$  is the fractional abundance of  $^{13}\text{C}^{18}\text{O}^{16}\text{O}_2$  at  $t = 0$ . Similar to equilibrium abundances, initial fractional  
575 abundances are independent of  $k$ . Equation A.6 is equivalent to (Passey and Henkes, 2012)

$$\frac{\Delta_{63}(k, t) - \Delta_{63}^{\text{eq}}(T)}{\Delta_{63}^0 - \Delta_{63}^{\text{eq}}(T)} = e^{-kt}, \quad (\text{A.7})$$

576 where, by analogy to Eq. 1,

$$\Delta_{63} = \left[ \left( \frac{R^{63}}{R^{*63}} - 1 \right) - \left( \frac{R^{62}}{R^{*62}} - 1 \right) - \left( \frac{R^{61}}{R^{*61}} - 1 \right) \right] \times 1000\text{‰}, \quad (\text{A.8})$$

577  $R^i = [i]/[60]$ , and  $R^{*i}$  denotes the  $R^i$  value for a stochastic isotopologue distribution (Schauble et al., 2006). Following  
 578 Guo et al. (2009), we let  $\Delta_{63} = \Delta_{47} - \Delta_{47}^*$ , where the phosphoric acid fractionation factor  $\Delta_{47}^*$  is approximately constant  
 579 for a given acid digestion temperature. Thus, Eq. A.7 is equal to

$$\frac{\Delta_{47}(k, t) - \Delta_{47}^{\text{eq}}(T)}{\Delta_{47}^0 - \Delta_{47}^{\text{eq}}(T)} = e^{-kt}. \quad (\text{A.9})$$

580 Utilizing the definition of  $g(k, t)$  from Eq. 3, this can be written as

$$g(k, t) = e^{-kt}. \quad (\text{A.10})$$

581 Although derivational details differ, this result is identical to that in Appendix A of Passey and Henkes (2012) for bulk  
 582  $\Delta_{47}(t)$  evolution assuming a single  $k$  value.

## 583 Appendix B. Relationship between reactions in parallel and in series

584 Stolper and Eiler (2015) treat the carbonate isotopologue reordering reaction as two processes occurring in series:  
 585 First, neighboring  $^{13}\text{C}^{18}\text{O}^{16}\text{O}_2$  and  $^{12}\text{C}^{16}\text{O}_3$  groups react to form a "pair". Then, paired  $^{13}\text{C}^{16}\text{O}_3$  and  $^{12}\text{C}^{18}\text{O}^{16}\text{O}_2$   
 586 groups diffuse to form "singletons". Following Eq. 16, the derivative of  $^{13}\text{C}^{18}\text{O}^{16}\text{O}_2$  and pair abundances with respect  
 587 to time is

$$\begin{aligned} \frac{d[63](t)}{dt} &= -k_1[60](t)[63](t) + \alpha_1 k_1 [p](t), \\ \frac{d[p](t)}{dt} &= k_1[60](t)[63](t) - (\alpha_1 k_1 + k_{\text{pd}})[p](t) + \alpha_{\text{pd}} k_{\text{pd}} [61]_s(t)[62]_s(t), \end{aligned} \quad (\text{B.1})$$

588 where  $[i]$  denotes the fractional abundance of atomic mass  $i$  and  $[p]$  denotes the fractional abundance of pairs such  
 589 that  $\sum_{i=60}^{63} [i] + [p] = 1$ . As above, we ignore contributions to each atomic mass by  $^{17}\text{O}$ -containing isotopologues (Wang  
 590 et al., 2004; Schauble et al., 2006). Similarly following Eq. 16, we have

$$\begin{aligned} \alpha_1(T) &= \frac{[60]_{\text{eq}}[63]_{\text{eq}}}{[p]_{\text{eq}}}, \\ \alpha_{\text{pd}}(T) &= \frac{[p]_{\text{eq}}}{[61]_{s,\text{eq}}[62]_{s,\text{eq}}}, \end{aligned} \quad (\text{B.2})$$

591 where the subscripts "eq" denotes equilibrium abundance at temperature  $T$  and the subscript "s" denotes singletons.  
 592 Because  $^{12}\text{C}^{16}\text{O}_3$ ,  $(^{13}\text{C}^{16}\text{O}_3)_s$  and  $(^{12}\text{C}^{18}\text{O}^{16}\text{O}_2)_s$  are orders-of-magnitude more abundant than pairs and  $^{13}\text{C}^{18}\text{O}^{16}\text{O}_2$   
 593 (Wang et al., 2004; Affek and Eiler, 2006; Stolper and Eiler, 2015), we again assume that changes in the concentrations  
 594 of these species are negligible and let

$$\begin{aligned} [60](t) &= [60]_{\text{eq}}, \\ [61]_s(t) &= [61]_{s,\text{eq}}, \\ [62]_s(t) &= [62]_{s,\text{eq}}. \end{aligned} \quad (\text{B.3})$$

595 Furthermore, we use the fact that  $G(t)$  is equivalent to

$$G(t) = \frac{[63](t) - [63]_{\text{eq}}}{[63]_0 - [63]_{\text{eq}}}, \quad (\text{B.4})$$

596 and we similarly define the reaction progress of pairs as

$$H(t) = \frac{[p](t) - [p]_{\text{eq}}}{[63]_0 - [63]_{\text{eq}}}, \quad (\text{B.5})$$

597 noting that the upper bound of  $H(t)$  depends on  $[63]_0$  and  $[63]_{\text{eq}}$  (i.e.,  $H(t)$  is not strictly bounded to  $[0, 1]$ ). By  
598 substituting Eqs. B.2–B.5 into Eq. B.1, the derivatives of reaction progress with respect to time can be simplified to

$$\begin{aligned} \frac{dG(t)}{dt} &= -k_1 G + \alpha_1 k_1 H, \\ \frac{dH(t)}{dt} &= k_1 G - (\alpha_1 k_1 + k_{\text{pd}}) H. \end{aligned} \quad (\text{B.6})$$

599 In matrix form, this becomes

$$\frac{d\mathbf{x}(t)}{dt} = \mathbf{B}\mathbf{x}(t), \quad (\text{B.7})$$

600 where

$$\mathbf{x}(t) = \begin{bmatrix} G(t) \\ H(t) \end{bmatrix}, \quad \mathbf{B} = \begin{bmatrix} -k_1 & \alpha_1 k_1 \\ k_1 & -(\alpha_1 k_1 + k_{\text{pd}}) \end{bmatrix}. \quad (\text{B.8})$$

601 The solution to Eq. B.8 is found by assuming solutions exist in the form (Forney and Rothman, 2014)

$$\mathbf{x}(t) = \begin{bmatrix} u_1 \\ u_2 \end{bmatrix} e^{-\lambda t}. \quad (\text{B.9})$$

602 Substituting Eq. B.9 into Eq. B.7 results in the eigenvalue problem

$$-\lambda \begin{bmatrix} u_1 \\ u_2 \end{bmatrix} = \begin{bmatrix} -k_1 & \alpha_1 k_1 \\ k_1 & -(\alpha_1 k_1 + k_{\text{pd}}) \end{bmatrix} \begin{bmatrix} u_1 \\ u_2 \end{bmatrix}, \quad (\text{B.10})$$

603 where  $\lambda$  must satisfy

$$\det(\mathbf{B} + \lambda \mathbf{I}) = 0, \quad (\text{B.11})$$

604 and  $\mathbf{I}$  is the  $2 \times 2$  identity matrix. Because  $\alpha_1 \gtrsim 1$  and  $(k_1 + k_{\text{pd}} + \alpha_1 k_1)^2 > 4k_1 k_{\text{pd}}$ , Eq. B.11 contains two real solutions,  
605  $\lambda_1$  and  $\lambda_2$ . Substituting these into Eq. B.10 yields the two eigenvectors,  $\mathbf{u}_1$  and  $\mathbf{u}_2$ . The solution to  $\mathbf{x}(t)$  is thus a  
606 superposition of both exponential decays (Forney and Rothman, 2014)

$$\mathbf{x}(t) = f_1 \mathbf{u}_1 e^{-\lambda_1 t} + f_2 \mathbf{u}_2 e^{-\lambda_2 t}, \quad (\text{B.12})$$

607 where the weighting factors  $f_1$  and  $f_2$  can be found by substituting the initial conditions  $G_0$  and  $H_0$  at  $t = 0$  into Eq.  
608 B.12;  $G_0 \equiv 1$  by definition whereas  $H_0$  is estimated based on mass spectrometric measurements of  $[63]_0$  and known

609 or assumed  $T$  vs.  $[63]_{\text{eq}}$  and  $T$  vs.  $[p]_{\text{eq}}$  relationships (e.g., Eqs. 2 and 17 in Bonifacie et al., 2017; Stolper and Eiler,  
610 2015, respectively). Focusing on  $G(t)$ , this can be written as

$$G(t) = \sum_{i=1}^2 r(\lambda_i) e^{-\lambda_i t}, \quad (\text{B.13})$$

611 where  $r(\lambda_i) = f_i u_{i,1}$  can be thought of as  $p(k_i)$  projected onto the eigenvectors (Forney and Rothman, 2014). Therefore,  
612 while Eq. 16 defines two reactions in series, the total isotopologue reordering reaction behaves as two reactions  
613 occurring in parallel.

### 614 Appendix C. A continuum of paired reaction-diffusion rates

615 By analogy to Eq. 8, suppose that each step in Eq. 16 is itself described by a parallel superposition of  $n$  reactions  
616 occurring at various rates. This allows  $\kappa_1(t)$  and  $\kappa_{\text{pd}}(t)$  in Eq. 16 to evolve with time. It follows that

$$G(t) = \sum_{i=0}^n p(k_i) g(k_i, t), \quad H(t) = \sum_{i=0}^n q(k_i) h(k_i, t), \quad (\text{C.1})$$

617 where  $p(k_i)$  and  $q(k_i)$  are the fractional contributions of each  $k_i$  to  $G(t)$  and  $H(t)$ , respectively, and

$$\sum_{i=1}^n p(k_i) \equiv 1, \quad \sum_{i=1}^n q(k_i) \equiv 1. \quad (\text{C.2})$$

618 Equation B.7 can be rewritten for the fraction of material associated with a given  $k$  as

$$\begin{aligned} \frac{dg(k_i, t)}{dt} &= -k_i g(k_i, t) + p(k_i) \alpha_1 \sum_{j=1}^n q(k_j) k_j h(k_j, t), \\ \frac{dh(k_i, t)}{dt} &= q(k_i) \sum_{j=1}^n p(k_j) k_j g(k_j, t) - \left( \alpha_1 \sum_{j=1}^n p(k_j) k_j + k_i \right) h(k_i, t). \end{aligned} \quad (\text{C.3})$$

619 Reaction progress again follows Eq. B.8 but with

$$\mathbf{x}(t) = \begin{bmatrix} \mathbf{g}(t) \\ \mathbf{h}(t) \end{bmatrix}, \quad (\text{C.4})$$

620 where

$$\begin{aligned} \mathbf{g}(t) &= [g(k_1, t), g(k_2, t), \dots, g(k_n, t)]^T, \\ \mathbf{h}(t) &= [h(k_1, t), h(k_2, t), \dots, h(k_n, t)]^T, \end{aligned} \quad (\text{C.5})$$

621 and  $\mathbf{B}$  is now a  $2n \times 2n$  matrix with each row calculated using Eq. C.3. As above,  $\mathbf{x}(t)$  can be found by assuming  
622 solutions in the form

$$\mathbf{x}(t) = \begin{bmatrix} u_1 \\ u_2 \\ \vdots \\ u_{2n} \end{bmatrix} e^{-\lambda t}. \quad (\text{C.6})$$

623 There now exist  $2n$  solutions with unique eigenvalues and eigenvectors. The overall solution is again a superposition  
 624 of all exponential decays (Forney and Rothman, 2014) calculated as

$$\mathbf{x}(t) = \mathbf{U}e^{-\mathbf{\Lambda}t}\mathbf{f}, \quad (\text{C.7})$$

625 where  $\mathbf{U}$  is the  $2n \times 2n$  matrix of eigenvectors,  $e$  is the matrix exponential,  $\mathbf{\Lambda}$  is the  $2n \times 2n$  diagonal matrix of  
 626 eigenvalues, and  $\mathbf{f}$  is the vector of weighting factors. As above,  $\mathbf{f}$  is found by substituting the initial conditions into  
 627 Eq. C.7:

$$\mathbf{f} = \mathbf{U}^{-1}\mathbf{x}_0, \quad (\text{C.8})$$

628 where

$$\mathbf{x}_0 = \begin{bmatrix} \mathbf{g}_0 \\ \mathbf{h}_0 \end{bmatrix}, \quad (\text{C.9})$$

629 and

$$\begin{aligned} \mathbf{g}_0 &= G_0 [p(k_1), p(k_2), \dots, p(k_n)]^T, \\ \mathbf{h}_0 &= H_0 [q(k_1), q(k_2), \dots, q(k_n)]^T. \end{aligned} \quad (\text{C.10})$$

630  $G_0$  and  $H_0$  are calculated as in Appendix B. Each entry in  $\mathbf{x}(t)$  is thus equal to

$$x_i(t) = f_i \sum_{j=1}^{2n} u_{j,i} e^{-\lambda_j t}. \quad (\text{C.11})$$

631 Again focusing solely on  $G(t)$  and recalling that the first  $n$  rows of  $\mathbf{x}(t)$  correspond to each  $g(k_i, t)$ , Eqs. C.1 and C.11  
 632 can be combined to give

$$G(t) = \sum_{i=1}^n r(\lambda_i) e^{-\lambda_i t}, \quad (\text{C.12})$$

633 where

$$r(\lambda_i) = p(k_i) f_i \sum_{j=1}^{2n} u_{j,i}. \quad (\text{C.13})$$

634 Equation C.12 is readily written in continuous form as

$$G(t) = \int_0^{\infty} r(\lambda) e^{-\lambda t}. \quad (\text{C.14})$$

635 Similar to the 2-component case (Appendix B), a system of two reactions in series—each of which following a  
 636 parallel superposition of first-order reactions at different rates—behaves itself as a superposition of reactions occurring  
 637 in parallel. A unique feature of serial reactions is that each  $r(\lambda_i)$  can be negative since this represents  $p(k)$  projected  
 638 onto eigenvectors whose entries need not be positive (Eq. C.13).

639 **Appendix D. Solving the inverse Laplace transform**

640 To numerically estimate  $\rho(v)$ , we first discretize  $t$  and  $G(t)$  into vectors  $\mathbf{t}$  and  $\mathbf{G}$  containing  $n_t$  nodes such that  
 641 each node corresponds to the time of each  $\Delta_{47}$  measurement (Forney and Rothman, 2012b; Hemingway et al., 2017).  
 642 Importantly, this does not require a uniform time step since experimental  $\Delta_{47}$  measurements are rarely uniformly  
 643 distributed in time. We similarly discretize  $v$  into a uniformly spaced vector  $\mathbf{v}$  containing  $n_v$  nodes such that

$$\Delta v = \frac{v_{\max} - v_{\min}}{n_v}, \quad (\text{D.1})$$

644 where we let  $v_{\min} = -60$  and  $v_{\max} = 20$  based on published data (Passey and Henkes, 2012; Henkes et al., 2014;  
 645 Stolper and Eiler, 2015; Brenner et al., 2018; Lloyd et al., 2018; Chen et al., 2019).

646 Equation 19 can be separated into two components: (i)  $\rho(v)$  and (ii) the Laplace transform operator  $e^{-e^v t}$ . We  
 647 discretize the Laplace transform operator into a  $n_t \times n_{nu}$  matrix  $\mathbf{A}$  such that

$$\begin{aligned} A_{i,j} &= \exp\left[-\exp(v_j) t_i\right] \Delta v, \\ i &= 1, \dots, n_t, \\ j &= 1, \dots, n_v. \end{aligned} \quad (\text{D.2})$$

648 Finally, we define  $\boldsymbol{\rho}$  to be the unknown, discretized vector of  $\rho(v)$  such that

$$\rho_j = \frac{1}{\Delta v} \int_{v_j - \frac{1}{2}\Delta v}^{v_j + \frac{1}{2}\Delta v} \rho(v) dv, \quad j = 1, \dots, n_v. \quad (\text{D.3})$$

649 Our model can thus be written in matrix form as

$$\mathbf{G} = \mathbf{A}\boldsymbol{\rho}. \quad (\text{D.4})$$

650 To find a "smoothed" solution using Tikhonov regularization, we additionally calculate the bi-diagonal first-derivative  
 651 operator matrix,  $\mathbf{R}$ . That is, we let

$$\left\| \frac{d\rho(v)}{dv} \right\| = \left[ \sum_{j=2}^{n_v-1} \left( \frac{\rho_{j+1} - \rho_j}{\Delta v} \right)^2 \right]^{\frac{1}{2}} \equiv \|\mathbf{R}\boldsymbol{\rho}\|, \quad (\text{D.5})$$

652 where the first and last rows of  $\mathbf{R}$  are set to  $[1 \quad \mathbf{0}]$  and  $[\mathbf{0} \quad -1]$ , respectively, and  $\mathbf{0}$  is the zero vector of length  $n_v - 1$ .  
 653 This forces the constraint that  $\boldsymbol{\rho} = 0$  outside of the range  $v_{\min} < v < v_{\max}$  (Forney and Rothman, 2012b).

654 **Appendix E. Deriving  $p(E)$  from  $\rho(v)$**

655 Suppose  $\rho(v) \sim \mathcal{N}(\mu_v, \sigma_v)$  and  $v = v_0 - E/RT$ , then the pdf of  $E$  can be readily calculated by change of variables.  
 656 That is,

$$\begin{aligned} p(E) &= \rho\{v(E)\} \left| \frac{dv}{dE} \right|, \\ &= \left( \frac{1}{\sqrt{2\pi}\sigma_v} \exp\left[-\frac{(v_0 - \frac{E}{RT} - \mu_v)^2}{2\sigma_v^2}\right] \right) \left| -\frac{1}{RT} \right|. \end{aligned} \quad (\text{E.1})$$

657 If we let

$$\begin{aligned}\mu_E &= RT(v_0 - \mu_v), \\ \sigma_E &= RT\sigma_v,\end{aligned}\tag{E.2}$$

658 then this simplifies to

$$p(E) = \frac{1}{\sqrt{2\pi}\sigma_E} \exp\left[-\frac{(E - \mu_E)^2}{2\sigma_E^2}\right],\tag{E.3}$$

659 which defines a normal distribution with mean  $\mu_E$  and standard deviation  $\sigma_E$ .

## 660 Appendix F. Supplementary data and figures

661 Supplementary data and figures associated with this article can be found in the online version at <http://xxxxxx>.

## 662 References

- 663 Affek, H.P., Eiler, J.M., 2006. Abundance of mass 47 CO<sub>2</sub> in urban air, car exhaust, and human breath. *Geochimica et Cosmochimica Acta* 70,  
664 1–12.
- 665 Bonifacie, M., Calmels, D., Eiler, J.M., Horita, J., Chaduteau, C., Vasconcelos, C., Agrinier, P., Katz, A., Passey, B.H., Ferry, J.M., Bourrand, J.J.,  
666 2017. Calibration of the dolomite clumped isotope thermometer from 25 to 350°C, and implications for a universal calibration for all (Ca, Mg,  
667 Fe)CO<sub>3</sub> carbonates. *Geochimica et Cosmochimica Acta* 200, 255–279.
- 668 Boudreau, B.P., Ruddick, B.R., 1991. On a reactive continuum representation of organic matter diagenesis. *American Journal of Science* 291,  
669 507–538.
- 670 Brenner, D.C., Passey, B.H., Stolper, D.A., 2018. Influence of water on clumped-isotope bond reordering kinetics in calcite. *Geochimica et*  
671 *Cosmochimica Acta* 224, 42–63.
- 672 Burnham, A.K., Braun, R.L., 1999. Global kinetic analysis of complex materials. *Energy & Fuels* 13, 1–22.
- 673 Chen, S., Ryb, U., Piasecki, A.M., Lloyd, M.K., Baker, M.B., Eiler, J.M., 2019. Mechanism of solid-state clumped isotope reordering in carbonate  
674 minerals from aragonite heating experiments. *Geochimica et Cosmochimica Acta* 258, 156–173.
- 675 Daëron, M., Blamart, D., Peral, M., Affek, H., 2016. Absolute isotopic abundance ratios and the accuracy of  $\Delta_{47}$  measurements. *Chemical Geology*  
676 442, 83–96.
- 677 Dennis, K.J., Affek, H.P., Passey, B.H., Schrag, D.P., Eiler, J.M., 2011. Defining an absolute reference frame for 'clumped' isotope studies of CO<sub>2</sub>.  
678 *Geochimica et Cosmochimica Acta* 75, 7117–7131.
- 679 Dennis, K.J., Schrag, D.P., 2010. Clumped isotope thermometry of carbonates as an indicator of diagenetic alteration. *Geochimica et Cosmochim-*  
680 *ica Acta* 74, 4110–4122.
- 681 Dodson, M.H., 1973. Closure temperature in cooling geochronological and petrological systems. *Contributions to Mineralogy and Petrology* 40,  
682 259–274.
- 683 Ehlers, T.A., 2005. Crustal thermal processes and the interpretation of thermochronometer data. *Reviews in Mineralogy and Geochemistry* 58,  
684 315–350.
- 685 Eiler, J.M., 2011. Paleoclimate reconstruction using carbonate clumped isotope thermometry. *Quaternary Science Reviews* 30, 3575–3588.
- 686 Eyring, H., 1935. The activated complex in chemical reactions. *Journal of Chemical Physics* 3, 107–115.
- 687 Ferry, J.M., Passey, B.H., Vasconcelos, C., Eiler, J.M., 2011. Formation of dolomite at 40–80°C in the latemar carbonate buildup, dolomites, Italy,  
688 from clumped isotope thermometry. *Geology* 39, 571–574.
- 689 Fiebig, J., Bajnai, D., Löffler, N., Methner, K., Krsnik, E., Mulch, A., Hofmann, S., 2019. Combined high-precision  $\Delta_{48}$  and  $\Delta_{47}$  analysis of  
690 carbonates. *Chemical Geology* 522, 186–191.

691 Finnegan, S., Bergmann, K., Eiler, J.M., Jones, D.S., Fike, D.A., Eisenman, I., Hughes, N.C., Tripathi, A.K., Fischer, W.W., 2011. The magnitude  
692 and duration of late ordovician–early silurian glaciation. *Science* 331, 903–906.

693 Forney, D.C., Rothman, D.H., 2012a. Common structure in the heterogeneity of plant-matter decay. *Journal of the Royal Society Interface* 9,  
694 2255–2267.

695 Forney, D.C., Rothman, D.H., 2012b. Inverse method for estimating respiration rates from decay time series. *Biogeosciences* 9, 3601–3612.

696 Forney, D.C., Rothman, D.H., 2014. Carbon transit through degradation networks. *Ecological Monographs* 84, 109–129.

697 Fosu, B.R., Ghosh, P., Viladkar, S.G., 2020. Clumped isotope geochemistry of carbonatites in the north-western deccan igneous province: Aspects  
698 of evolution, post-depositional alteration and mineralisation. *Geochimica et Cosmochimica Acta* 274, 118–135.

699 Ghosh, P., Adkins, J., Affek, H., Balta, B., Guo, W., Schauble, E.A., Schrag, D., Eiler, J.M., 2006.  $^{13}\text{C}$ – $^{18}\text{O}$  bonds in carbonate minerals: A new  
700 kind of paleothermometer. *Geochimica et Cosmochimica Acta* 70, 1439–1456.

701 Guo, W., Mosenfelder, J.L., Goddard III, W.A., Eiler, J.M., 2009. Isotopic fractionations associated with phosphoric acid digestion of carbonate  
702 minerals: Insights from first-principles theoretical modeling and clumped isotope measurements. *Geochimica et Cosmochimica Acta* 73, 7203–  
703 7225.

704 Hansen, P.C., 1994. Regularization tools: a matlab package for analysis and solution of discrete ill-posed problems. *Numerical Algorithms* 6,  
705 1–35.

706 Hemingway, J.D., 2020. *isotopylog*: Open-source tools for clumped isotope kinetic data analysis, 2020-. URL:  
707 <http://pypi.python.org/pypi/isotopylog>.

708 Hemingway, J.D., Rothman, D.H., Rosengard, S.Z., Galy, V.V., 2017. Technical note: An inverse method to relate organic carbon reactivity to  
709 isotope composition from serial oxidation. *Biogeosciences* 14, 5099–5114.

710 Henkes, G.A., Passey, B.H., Grossman, E.L., Shenton, B.J., Pérez-Huerta, A., Yancey, T.E., 2014. Temperature limits for preservation of primary  
711 calcite clumped isotope paleotemperatures. *Geochimica et Cosmochimica Acta* 139, 362–382.

712 Henkes, G.A., Passey, B.H., Grossman, E.L., Shenton, B.J., Yancey, T.E., Pérez-Huerta, A., 2018. Temperature evolution and the oxygen isotope  
713 composition of phanerozoic oceans from carbonate clumped isotope thermometry. *Earth and Planetary Science Letters* 490, 40–50.

714 Henkes, G.A., Passey, B.H., Wanamaker Jr, A.D., Grossman, E.L., Ambrose Jr, W.G., Carroll, M.L., 2013. Carbonate clumped isotope compositions  
715 of modern marine mollusk and brachiopod shells. *Geochimica et Cosmochimica Acta* 106, 307–325.

716 Huber, D., 1985. Statistical model for stretched exponential relaxation in macroscopic systems. *Physical Review B* 31, 6070–6071.

717 Huntington, K.W., Budd, D.A., Wernicke, B.P., Eiler, J.M., 2011. Use of clumped-isotope thermometry to constrain the crystallization temperature  
718 of diagenetic calcite. *Journal of Sedimentary Research* 81, 656–669.

719 Ku, H.H., 1966. Notes on the use of propagation of error formulas. *Journal of Research of the National Bureau of Standards* 70, 263–273.

720 Lawson, C.L., Hanson, R.J., 1995. Solving least squares problems. volume 15. Siam.

721 Lawson, M., Shenton, B.J., Stolper, D.A., Eiler, J.M., Rasbury, E.T., Becker, T.P., Phillips-Lander, C.M., Buono, A.S., Becker, S.P., Pottorf, R.,  
722 Gray, G.G., Yurewicz, D., Gournay, J., 2018. Deciphering the diagenetic history of the el abra formation of eastern mexico using reordered  
723 clumped isotope temperatures and u-pb dating. *GSA Bulletin* 130, 617–629.

724 Lloyd, M.K., Eiler, J.M., Nabelek, P.I., 2017. Clumped isotope thermometry of calcite and dolomite in a contact metamorphic environment.  
725 *Geochimica et Cosmochimica Acta* 197, 323–344.

726 Lloyd, M.K., Ryb, U., Eiler, J.M., 2018. Experimental calibration of clumped isotope reordering in dolomite. *Geochimica et Cosmochimica Acta*  
727 242, 1–20.

728 Marquardt, D.W., 1963. An algorithm for least-squares estimation of nonlinear parameters. *Journal of the society for Industrial and Applied*  
729 *Mathematics* 11, 431–441.

730 Miller, H.B., Farley, K.A., Vasconcelos, P.M., Mostert, A., Eiler, J.M., 2020. Intracrystalline site preference of oxygen isotopes in goethite: A  
731 single-mineral paleothermometer. *Earth and Planetary Science Letters* 539, 116237.

732 Montroll, E.W., Shlesinger, M.F., 1982. On  $1/f$  noise and other distributions with long tails. *Proceedings of the National Academy of Sciences* 79,  
733 3380–3383.

734 Neubauer, C., Crémière, A., Wang, X.T., Thiagarajan, N., Sessions, A.L., Adkins, J.F., Dalleska, N.F., Turchyn, A.V., Clegg, J.A., Moradian,  
735 A., Sweredoski, M.J., Garbis, S.D., Eiler, J.M., 2020. Stable isotope analysis of intact oxyanions using electrospray quadrupole-orbitrap mass  
736 spectrometry. *Analytical Chemistry* 92, 3077–3085.

737 Passey, B.H., Henkes, G.A., 2012. Carbonate clumped isotope bond reordering and geospeedometry. *Earth and Planetary Science Letters* 351,  
738 223–236.

739 Passey, B.H., Levin, N.E., Cerling, T.E., Brown, F.H., Eiler, J.M., 2010. High-temperature environments of human evolution in east africa based  
740 on bond ordering in paleosol carbonates. *Proceedings of the National Academy of Sciences* 107, 11245–11249.

741 Quade, J., Eiler, J., Daeron, M., Achyuthan, H., 2013. The clumped isotope geothermometer in soil and paleosol carbonate. *Geochimica et*  
742 *Cosmochimica Acta* 105, 92–107.

743 Ross, J., Vlad, M.O., 1999. Nonlinear kinetics and new approaches to complex reaction mechanisms. *Annual Reviews of Physical Chemistry* 50,  
744 51–78.

745 Ryb, U., Eiler, J.M., 2018. Oxygen isotope composition of the phanerozoic ocean and a possible solution to the dolomite problem. *Proceedings of*  
746 *the National Academy of Sciences* 115, 6602–6607.

747 Ryb, U., Lloyd, M., Stolper, D., Eiler, J., 2017. The clumped-isotope geochemistry of exhumed marbles from naxos, greece. *Earth and Planetary*  
748 *Science Letters* 470, 1–12.

749 Schauble, E.A., Ghosh, P., Eiler, J.M., 2006. Preferential formation of  $^{13}\text{C}$ - $^{18}\text{O}$  bonds in carbonate minerals, estimated using first-principles lattice  
750 dynamics. *Geochimica et Cosmochimica Acta* 70, 2510–2529.

751 Shenton, B.J., Grossman, E.L., Passey, B.H., Henkes, G.A., Becker, T.P., Laya, J.C., Perez-Huerta, A., Becker, S.P., Lawson, M., 2015. Clumped  
752 isotope thermometry in deeply buried sedimentary carbonates: The effects of bond reordering and recrystallization. *GSA Bulletin* 127, 1036–  
753 1051.

754 Stolper, D.A., Eiler, J.M., 2015. The kinetics of solid-state isotope-exchange reactions for clumped isotopes: A study of inorganic calcites and  
755 apatites from natural and experimental samples. *American Journal of Science* 315, 363–411.

756 Ueno, Y., Katsuta, T., Ishimaru, T., Yoshida, N., 2019. A new method for measuring  $^{34}\text{S}$ - $^{18}\text{O}$  clumping in sulfate, in: *Goldschmidt Conference*  
757 *Abstracts*.

758 Wang, Z., Schauble, E.A., Eiler, J.M., 2004. Equilibrium thermodynamics of multiply substituted isotopologues of molecular gases. *Geochimica*  
759 *et Cosmochimica Acta* 68, 4779–4797.

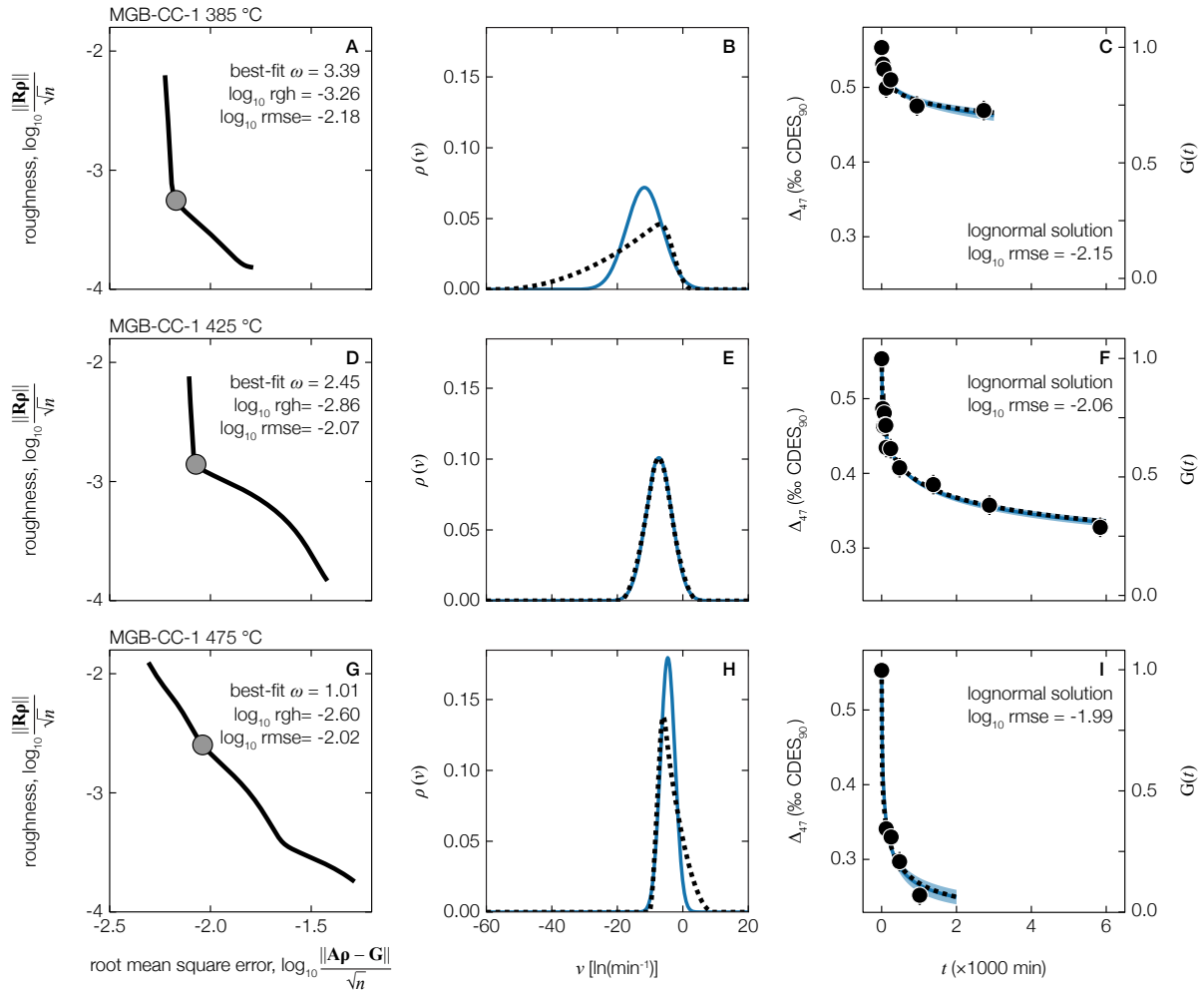


Figure 1: Examples of the disordered kinetic model for optical calcite (MGB-CC-1) isotopologue reordering experiments performed at (**top**) 385, (**middle**) 425, and (**bottom**) 475 °C (data from Passey and Henkes, 2012). Panels **A**, **D**, and **G** show the Tikhonov regularization L-curve for each experiment (solid black line), including the best-fit  $\omega$  value (gray circle). Panels **B**, **E**, and **H** show the pdf of  $\nu$  for each experiment, including the best-fit regularized inverse solution (dotted black line) and the lognormal solution (solid blue line). Panels **C**, **F**, and **I** show the measured  $\Delta_{47}$  values and the modeled  $\Delta_{47}$  evolution as predicted by the best-fit regularized inverse solution (dotted black line) and the lognormal solution (solid blue line). Shaded blue region is the propagated  $\pm 1\sigma$  uncertainty of the lognormal solution. For reference, reaction progress for each experiment is also shown by converting  $\Delta_{47}$  to  $G(t)$ . The observed left-skewed regularized inverse solution at lower temperature and right-skewed regularized inverse solution at higher temperature is a general feature of most experiments included in this study (Section 4.1). rgh = roughness; rmse = root mean square error, min = minutes.

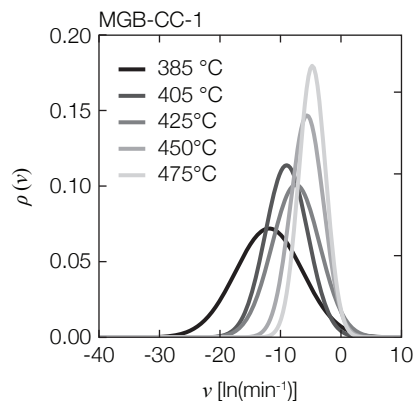


Figure 2: Rate distribution results for optical calcite (MGB-CC-1) isotopologue reordering experiments (data from Passey and Henkes, 2012). Best-fit lognormal rate distributions  $\rho(v)$  are shown for each experimental temperature (see Table S.3 for distribution statistics). Distributions generally become narrower and shift toward faster rates with increasing temperature, as predicted by Eq. 27 if isotopologue reordering follows an underlying Gaussian distribution of activation energies.

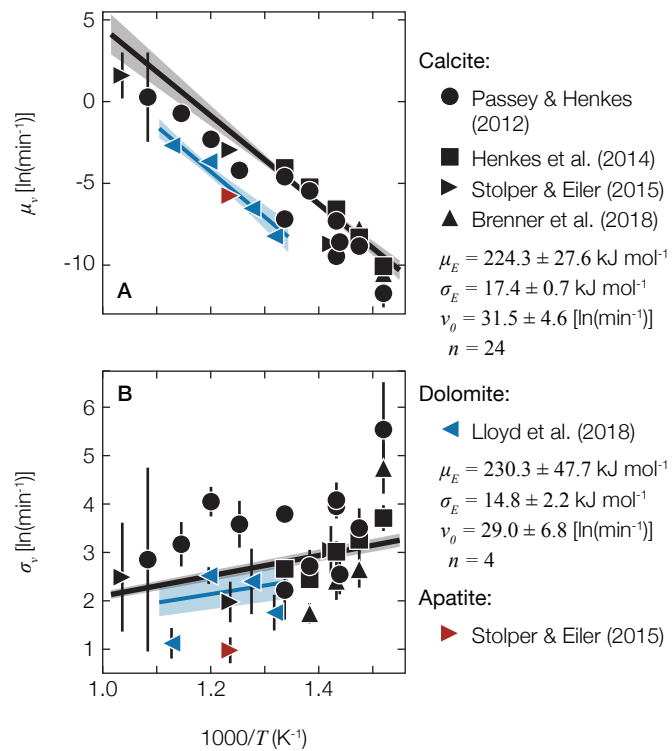


Figure 3: Arrhenius plots showing (A)  $\mu_v$  and (B)  $\sigma_v$  as a function of inverse experimental temperature. Arrhenius regression best-fit lines calculated using Eq. 27 for calcite (solid black line) and dolomite (solid blue line) are also shown, including  $\pm 1\sigma$  uncertainty about each regression line (shaded regions). Experiments exhibiting noisy data [i.e.,  $\Delta_{47}(t)$  signal-to-noise  $< 5$ ] or non-monotonic  $\Delta_{47}(t)$  evolution were excluded from regressions and thus are not shown here (see Sec. 4.3 and Table S.3).

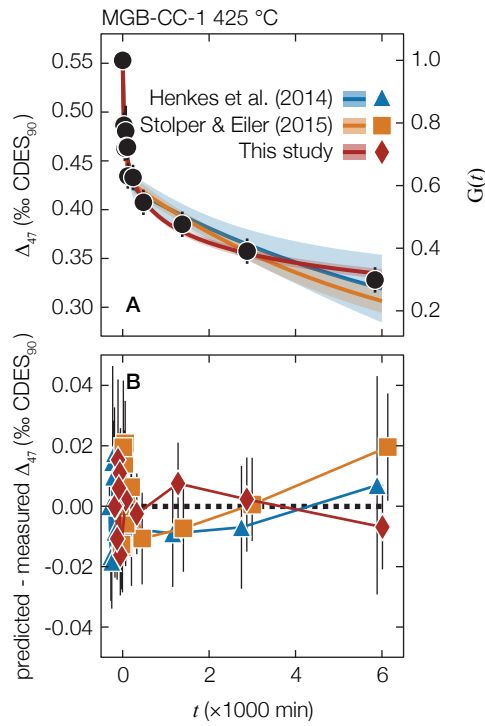


Figure 4: Example model fit comparison for an optical calcite (MGB-CC-1) heating experiment performed at 425 °C showing (A) measured and predicted  $\Delta_{47}$  evolution trends and (B) predicted – measured  $\Delta_{47}$  evolution misfit for each model (data from Passey and Henkes, 2012). Fit statistics for each model are as follows: transient defect/equilibrium defect (blue; Henkes et al., 2014),  $\log_{10}$  rmse =  $-1.94$ ; paired reaction-diffusion (orange; Stolper and Eiler, 2015),  $\log_{10}$  rmse =  $-1.92$ ; lognormal disordered kinetics (red; this study),  $\log_{10}$  rmse =  $-2.06$ . Shading in A represents model parameter  $\pm 1\sigma$  uncertainty. Model results in B are staggered slightly along the  $t$  axis for error bar visual clarity.

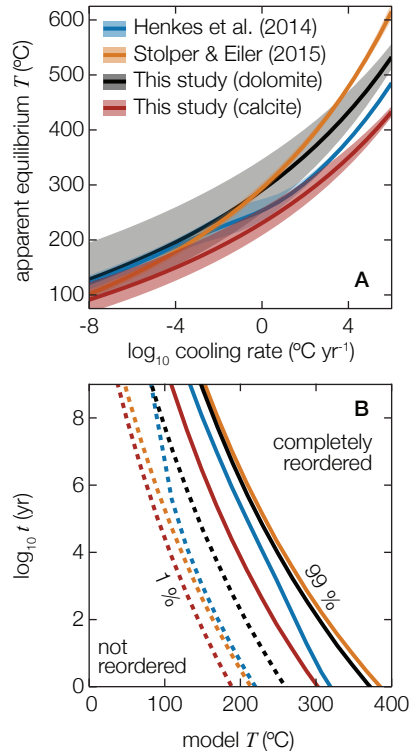


Figure 5: Isotopologue reordering diagnostic plots. **(A)** Apparent equilibrium temperature,  $T(\Delta_{47})_{ae}$ , for a variety of cooling rates. To generate each line,  $\Delta_{47}$  is initially in equilibrium at an arbitrarily high temperature, which then decreases linearly at a given rate.  $T(\Delta_{47})_{ae}$  at each cooling rate is determined using the calculated apparent equilibrium  $\Delta_{47}$  value for that rate. **(B)** Time-temperature fields for  $\Delta_{47}$  preservation. To generate each line, material that is initially described by  $T(\Delta_{47}) = 25$  °C is assumed to be instantaneously heated and held at a given temperature; dotted lines indicate the time until incipient (1%) isotopologue reordering, which is conservative and may be below the detection limit given typical precision on natural samples, whereas solid lines indicate the time until complete (99%) isotopologue reordering at that temperature. Colors indicate predictions using the kinetic values for each model as reported in their original publications: blue = transient defect/equilibrium defect (Henkes et al., 2014), orange = paired reaction-diffusion (Stolper and Eiler, 2015), black = dolomite lognormal disordered kinetics (this study), red = calcite lognormal disordered kinetics (this study). Shading in **A** represents model parameter  $\pm 1\sigma$  uncertainty.

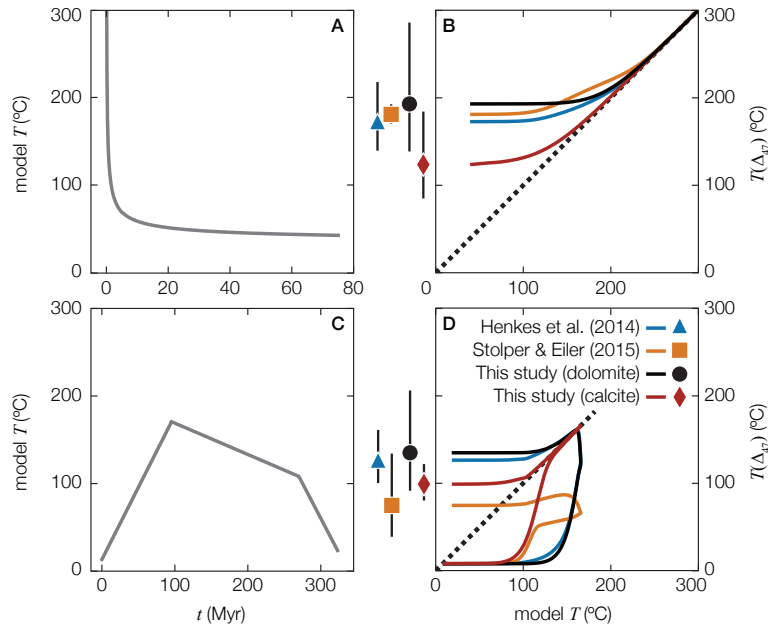


Figure 6: Thermal histories and corresponding carbonate  $T(\Delta_{47})$  evolution for two hypothetical scenarios: (A–B) a 1D thermal diffusion conductive model to approximate cooling of igneous or metamorphic rocks (adapted from Ehlers, 2005, for a 550 °C intrusion 3 km in diameter that cools by thermal diffusion with 30 °C country rock with a diffusivity of  $30 \text{ km}^2 \text{ Ma}^{-1}$ ), and (C–D) a low-resolution burial temperature history of sedimentary carbonate formed at 25 °C in a late Paleozoic foreland basin (adapted from Shenton et al., 2015). Panels A and C show imposed  $t-T$  histories whereas panels B and D show  $T(\Delta_{47})$  as predicted by various reordering models plotted against imposed model  $T$ . All models in B predict closure temperature-like behavior, whereas the  $T-T$  pathways in D are more complex and exhibit three distinctive features: (i) the temperature of incipient isotopologue bond reordering, (ii) the rate of approach to equilibrium (shown as a dotted 1 : 1 line), and (iii) the final  $T(\Delta_{47})_{ae}$  (shown to the left of the y-axis, including  $\pm 1\sigma$  model uncertainty). Colors indicate predictions using the kinetic values for each model as reported in their original publications: blue = transient defect/equilibrium defect (Henkes et al., 2014), orange = paired reaction-diffusion (Stolper and Eiler, 2015), black = dolomite lognormal disordered kinetics (this study), red = calcite lognormal disordered kinetics (this study).

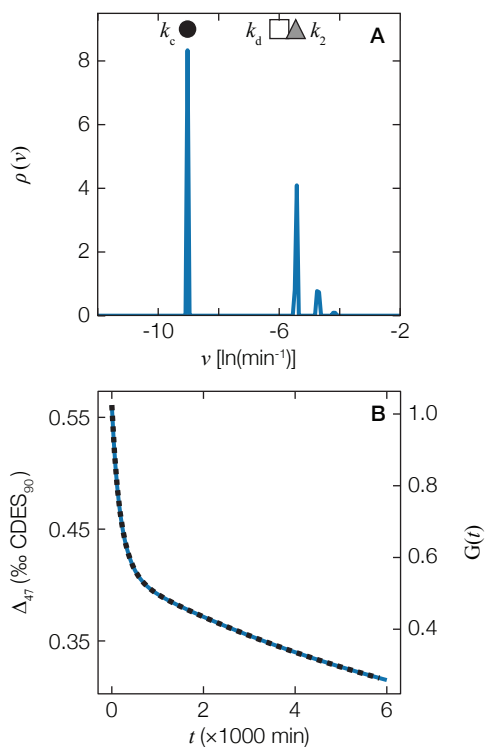


Figure S.1: Example demonstrating that the "transient defect/equilibrium defect" model (Henkes et al., 2014) is consistent with disordered kinetics. Henkes et al. (2014)  $k$  values for the model fit to an optical calcite (MGB-CC-1) isotopologue reordering experiment at 425 °C [symbols in **A**; in Henkes et al. (2014) notation; data from their Table B2] were used to generate a  $\Delta_{47}$  evolution trajectory (dotted black line in **B**). The inverse Laplace transform was then determined from this trajectory, leading to the pdf of  $v$  in **A** and the corresponding forward-modeled  $\Delta_{47}$  trajectory in **B** (solid blue lines). Both  $\Delta_{47}$  trajectories are identical, demonstrating that the Henkes et al. (2014) model is perfectly recreated by disordered kinetics. For reference, reaction progress is also shown by converting  $\Delta_{47}$  to  $G(t)$ .

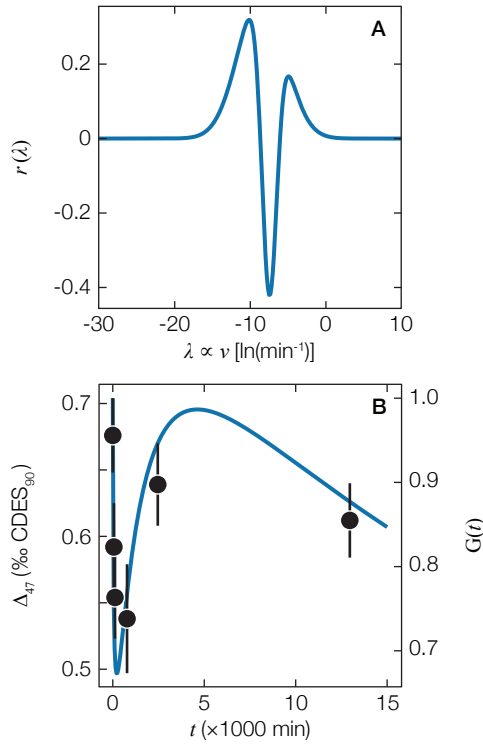


Figure S.2: Heuristic example showing how disordered kinetic processes in series can generate transient  $\Delta_{47}$  increases, as observed during aragonite isotopologue reordering experiments (Chen et al., 2019). The pdf of  $\lambda$  in **A** was generated as the difference between two arbitrary Gaussian distributions, with the first as  $\mathcal{N}(-8.5, 3)$  and the second as  $\mathcal{N}(-7.5, 1)$ . Importantly,  $r(\lambda)$  contains negative area. Panel **B** shows the  $G(t)$  evolution predicted by this  $r(\lambda)$  distribution (solid blue line). For reference, we overlay the  $\Delta_{47}$  evolution from a Tazouta aragonite reordering experiment performed at 300 °C [data from Chen et al. (2019); samples AP-4 through AP-D6 in their Table 1]. While this  $r(\lambda)$  distribution is arbitrary and was not generated from an inversion of the data, it clearly captures the main features of the measured  $\Delta_{47}$  evolution.

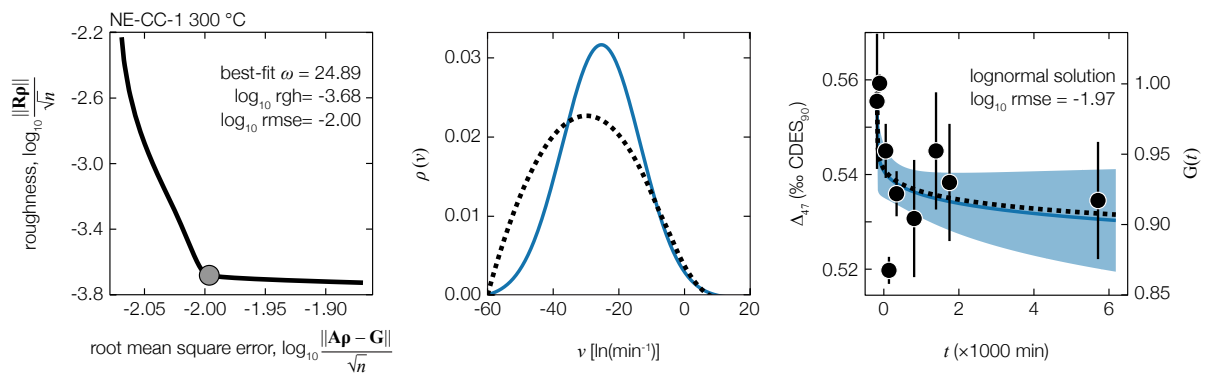


Figure S.3: Same as Fig. 1, but calculated using the spar calcite (NE-CC-1) isotopologue reordering experiment performed at 300 °C (data from Passey and Henkes, 2012). **(A)** Tikhonov regularization L-curve (solid black line), including the best-fit  $\omega$  value (gray circle). **(B)** pdf of  $\nu$ , including the best-fit regularized inverse solution (dotted black line) and the lognormal solution (solid blue line). **(C)** measured  $\Delta_{47}$  values and the modeled  $\Delta_{47}$  evolution as predicted by the best-fit regularized inverse solution (dotted black line) and the lognormal solution (solid blue line). Shaded blue region is the propagated  $\pm 1\sigma$  uncertainty of the lognormal solution. For reference, reaction progress is also shown by converting  $\Delta_{47}$  to  $G(t)$ . The model fit is poor for this experiment due to the low analytical signal-to-noise ratio, leading to large model uncertainty and an overly broad, left-skewed inverse solution for  $\rho(\nu)$ ; as such, this experiment was omitted from the final dataset. rgh = roughness; rmse = root mean square error, min = minutes.

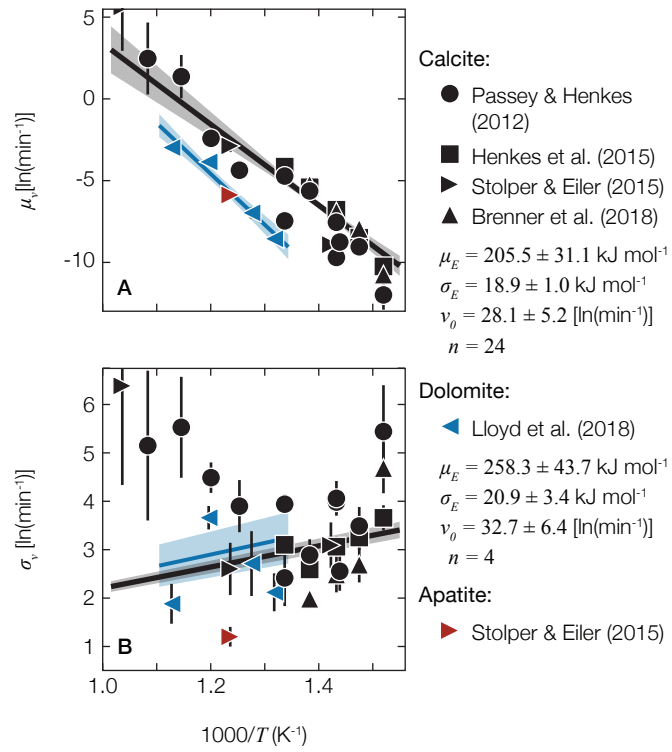


Figure S.4: Same as Fig. 3, but calculated using the  $T$  vs.  $\Delta_{47}^{\text{eq}}(T)$  relationship from Lloyd et al. (2018) (their Eq. 4). **(A)**  $\mu_v$  and **(B)**  $\sigma_v$  as a function of inverse experimental temperature. Arrhenius regression best-fit lines calculated using Eq. 27 for calcite (solid black line) and dolomite (solid blue line) are also shown, including  $\pm 1\sigma$  uncertainty about each regression line (shaded regions). Experiments exhibiting noisy data [i.e.,  $\Delta_{47}(t)$  signal-to-noise  $< 5$ ] or non-monotonic  $\Delta_{47}(t)$  evolution were excluded from regressions and thus are not shown here (see Sec. 4.3 and Table S.3).

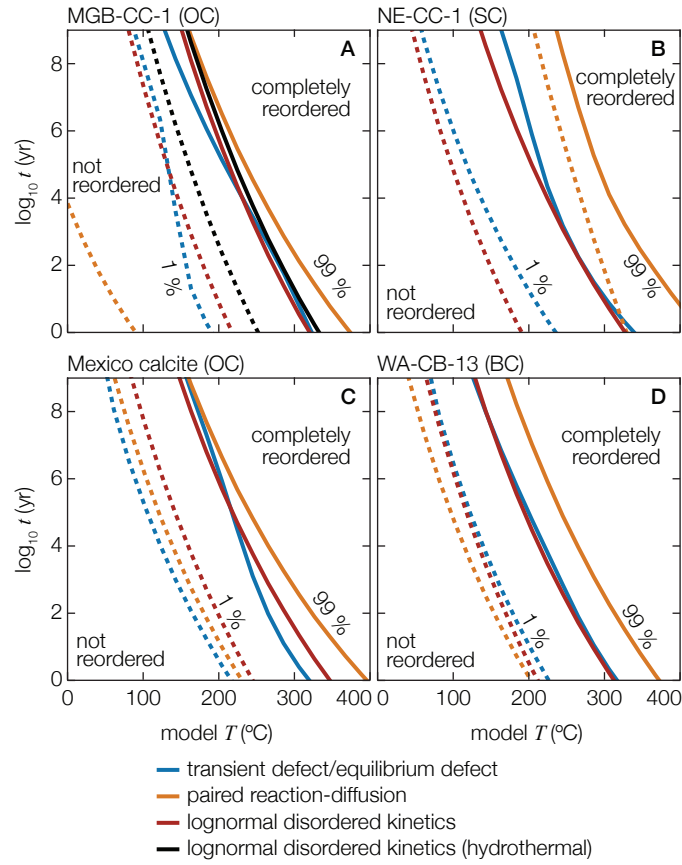


Figure S.5: Time-temperature fields for  $\Delta_{47}$  preservation. Same as Fig. 5B, but calculated here for individual calcite minerals: **(A)** MGB-CC-1 optical calcite (data from Passey and Henkes, 2012), **(B)** NE-CC-1 spar calcite (data from Passey and Henkes, 2012), **(C)** Mexican optical calcite (data from Stolper and Eiler, 2015), **(D)** WA-CB-13 brachiopod shell calcite (data from Henkes et al., 2014). To generate each line, material that is initially described by  $T(\Delta_{47}) = 25^{\circ}\text{C}$  is assumed to be instantaneously heated and held at a given temperature; dotted lines indicate the time until incipient (1%) isotopologue reordering, which is conservative and may be below the detection limit given typical precision on natural samples, whereas solid lines indicate the time until complete (99%) isotopologue reordering at that temperature. Where available, predictions were generated using kinetic values for each model as reported in their original publications (Henkes et al., 2014; Stolper and Eiler, 2015). In some cases, model parameters for certain minerals have not been previously reported (transient defect/equilibrium defect: NE-CC-1, Mexican optical calcite; paired reaction-diffusion: NE-CC-1) and were calculated here by fitting the original heating experiment data using the 'isotopolog' python package (Hemingway, 2020). blue = transient defect/equilibrium defect (Henkes et al., 2014), orange = paired reaction-diffusion (Stolper and Eiler, 2015), black = lognormal disordered kinetics, hydrothermal conditions (this study; sample MGB-CC-1 only; data from Brenner et al., 2018), red = lognormal disordered kinetics (this study).

Table S.1: All heating experiment metadata (sample ID, mineralogy, time, temperature, reference) and stable isotope data ( $\delta^{13}\text{C}$ ,  $\delta^{18}\text{O}$ ,  $\Delta_{47}$ ,  $\Delta_{47}$  uncertainty) used in this study. Where applicable,  $\Delta_{47}$  values are presented both in their original reference frame as well as in the CDES<sub>90</sub> reference frame.

Table S.2: Descriptions of all mathematical symbols used throughout this study.

Table S.3: Resulting statistics of regularized inverse (rmse, roughness norm,  $\omega$ ) and lognormal (rmse,  $\mu_v$ ,  $\sigma_v$ ) model fits for all heating experiments used in this study. The non-negativity constraint was relaxed for aragonite experiments [i.e.,  $r(\lambda)$  was fit]; thus, only regularized inverse model fit statistics are included for these experiments.